

Instantiations of Multiscale Kinship in Pressing-Defect Distributions in Yttria-Stabilized Zirconias by Powder Partitioning

Raíssa Monteiro Pereira, Ulrich Lohbauer, Christian Schulbert, Mathias Göken, Michael Wurmshuber, Tiago Bastos Moreira Campos, Gilmar Patrocínio Thim, Björn Mieller, and Renan Belli*

Modern dry pressing of ceramic powders using spray-dried granulates cannot avoid the occurrence of defects related to persisting inter- and intra-granulate interstitial voids. These constitute the parent defect size population limiting the application of polycrystalline ceramics in high-stress conditions. The mitigation of such defects could widen the range of application in technical and biomedical engineering, reduce the safety range for design, and extend the lifetime of components. Herein, the Weibull size-effect on strength in size-partitioned Yttria-stabilized zirconias (YSZ) feedstocks is used to explore the viability of changing the density distribution of granulate sizes as an effective strategy to obtain a denser particle packing that could reduce the size distribution of strength-limiting pressing defects. In a direct assessment of critical defect size using multiscale strength testing with a dataset of ≈ 1300 values, the success of such an approach in increasing the strength reliability for small volume components is demonstrated, along with its ultimate failure in altering the defect size distribution in sintered YSZ ceramics across several length scales. Finally, it is shown that granule morphology (spherical or dimpled) fails to affect the defect density and size distribution in YSZ ceramics.


1. Introduction

A persisting problem in ceramic manufacturing is the ubiquity of pressing defects in green bodies that resist densification sintering. Progress in powder technology via use of optimized slurry dispersants, plasticizers, binders, and emulsifiers, compounded to advances in spray-drying techniques and pressing strategies, ultimately improved compaction and reduced the broad array of multiple defect natures down to a small-sized defect population of narrower distribution.^[1–4] The elimination of formerly large and wide defect populations substantially improved mechanical performance and reliability; yet, remaining pressing defects are strength limiting at the upper range of strength notwithstanding. Reducing or eliminating such defects is of great interest for technical and biomedical engineering applications.

In modern feedstock powder dry-pressed compacts, that enduring small-sized narrow defect type becomes the parent

R. M. Pereira, U. Lohbauer, R. Belli
Forschungslabor für dentale Biomaterialien
Zahnklinik 1-Zahnerhaltung und Parodontologie
Friedrich-Alexander-Universität Erlangen-Nürnberg (FAU)
Glueckstraße 11, 91054 Erlangen, Germany
E-mail: renan.belli@fau.de

R. M. Pereira, T. B. M. Campos, G. P. Thim
Engenharia de Materiais
Instituto Tecnológico Aeronáutico (ITA)
Praça Marechal Eduardo Gomes 50, 12228-901 São José dos Campos,
Brazil

 The ORCID identification number(s) for the author(s) of this article can be found under <https://doi.org/10.1002/adem.202400139>.

© 2024 The Authors. Advanced Engineering Materials published by Wiley-VCH GmbH. This is an open access article under the terms of the Creative Commons Attribution-NonCommercial License, which permits use, distribution and reproduction in any medium, provided the original work is properly cited and is not used for commercial purposes.

DOI: 10.1002/adem.202400139

C. Schulbert
GeoZentrum Nordbayern, Paleontology
Friedrich-Alexander-Universität Erlangen-Nürnberg (FAU)
Loewenichstraße 28, 91054 Erlangen, Germany

M. Göken, M. Wurmshuber
Materials Science and Engineering, Institute I
Friedrich-Alexander-Universität Erlangen-Nürnberg (FAU)
Martensstraße 5, 91058 Erlangen, Germany

B. Mieller
Advanced Multi-Materials Processing
Bundesanstalt für Materialforschung und -prüfung (BAM)
Unter den Eichen 44-46, 12203 Berlin, Germany

population in the form of (i) ellipsoid-shaped intragranular porosity (IP), semi-circular shallow bowl-shaped concave planes (CP), and unfilled polyhedral-shaped interstitial junction vertices (IJV), as brilliantly illustrated by Okuma et al.^[5] for an alumina feedstock by multiscale synchrotron X-Ray computer tomography. While IP-defects are dispersed, small (<5 μm) and rounded, CP are sharp and wide (up to 60 μm) resulting from compaction of dimpled granules and oriented perpendicular to the pressing direction. Especially harmful, IJV-defects (20–50 μm) are created during the end stage of deformation of typical spherical spray-dried granulates having stiff binder shells,^[6] taking the tridimensional shape of a crowfoot with sharp “spikes” that get invariably oriented in unfavorable directions relative to any applied stress field: a predisposing setting for acting as fracture origin. It is not rare for multiple neighboring IJV-defects to connect forming long spanning defect networks of >100 μm.^[5]

The problem of pressing defects has been tackled from various angles, e.g.: 1) by modifying pressing procedures to include force vectors that change the shape of defects to less harmful forms;^[7] 2) by changing the constitution and plasticity of granulates to allow more homogeneous deformation during pressing, e.g., through optimization of spray-drying procedures^[8,9] as attempted with spray freeze-dried powders;^[10,11] 3) by devising mixing and pouring techniques that optimize granule packing configuration; and 4) by maximizing packing density through tailoring the granulate powder size distribution to reduce the ab initio volume size of interstitial voids,^[12–14] among others. Although these approaches have been somewhat attempted experimentally, they are far from being exhausted.

Here we explore the viability of strategy (4), namely, of changing the distribution of granulate sizes as an effective strategy to obtain a denser particle packing that could reduce the size distribution of strength-limiting pressing defects. Instead of using model powders, we partition the powder-size distribution of commercial feedstocks of Yttria-stabilized zirconias (YSZ) through cost-effective sieving processes. We first hypothesize that altering the granulate size distribution (narrower, shifted toward smaller or larger granulate sizes, and mixtures) affects the size distribution of pressing defects after dry pressing as a

direct consequence of packing density (and spatial distribution) of the ab initio interparticle interstitial spacing. This involves the classical problem of sphere packing in a practical application. Assuming that granule morphology may alter the packing arrangement, its effect is addressed here by employing a 3 mol% stabilized zirconia (3YSZ) powder composed of spherical granules and a 5 mol% stabilized zirconia (5YSZ) powder exhibiting dimpled granules (see **Figure 1**).

In one precedent worth noting,^[15] IJV-defects (of 40–100 μm in size) have been identified as the main defect type leading to failure of biomedical presintered dry-pressed zirconia compacts, being passed on to the sintered material accompanied by a shrinkage of one order of magnitude in critical size. Interestingly, past a certain threshold in effective volume/surface, the size of IJV-defects ceased to comply with the Weibull prediction for strength for large specimens. This was conjectured to lie on the limit of granulate sizes within the corresponding granulate size distribution, which could not produce ever larger IJV-defects. The testing for the sample-size effect on strength instantiates the distribution of pressing defects across several length scales, establishing the compliance or not to a Weibull prediction. Following on that approach (fracture statistics) in respect to pressing defects, as opposed to common optical defect screening methods, we demonstrate here this effect and report the limitations of tailoring the granulate size distribution of the feedstock in reducing the defect size distributions in both 3YSZ and 5YSZ ceramics and its independence of granule shape.

2. Results and Discussion

2.1. Granule Morphology

The as-delivered 3YSZ and 5YSZ powders revealed contrasting morphologies under the scanning electron microscopy (SEM) (see **Figure 1**). While the 3YSZ granules are predominantly spherical, granules in 5YSZ are dimpled and shaped irregular. That dimpled shape can often be found in spray-dried ceramic granules. A common model^[16] describes the granule shape development as follows: after droplet formation in the spray

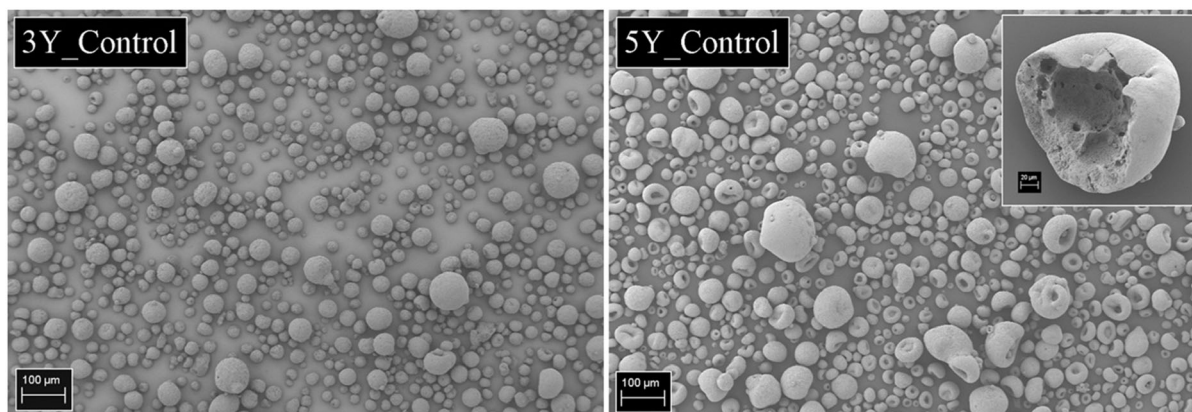


Figure 1. Scanning Electron Microscopy images of the 3YSZ (left hand-side) and 5YSZ (right hand-side) Control granulate powders before sieving. Note the difference in granulate geometry, with the 3YSZ powder showing mostly spherical shape, while the shape in 5YSZ is predominantly dimpled-spherical (one-sided donut). The inset shows a fractured granulate revealing the hollow interior. Note how the 5YSZ powder exhibits single larger granules compared to 3YSZ.

dryer, the rapid drying of the droplet surface leads to shrinkage and the formation of a hard shell. This shell stabilizes and prevents further shrinkage. As the drying process progresses, primary particles migrate from the interior of the droplet to the tightly packed shell, decreasing the particle density in the center. This creates a void and negative pressure inside the granule as the solvent further evaporates through the shell, leading to the collapse of the shell forming a dimple. Differences in the properties of the spray slurry and processing parameters will control whether granule collapse will take place or not; our observations suggest that the manufacturer, Tosoh, must thus employ different processes for these granulates or the 3Y and 5Y slurries have different properties. Even though no broken granules were seen in 3YSZ which could reveal their inner morphology (see inset in Figure 1 for hollow 5YSZ granule), some rare dimpled granulates in 3YSZ were found, hinting to the presence of a hollow interior as well, though apparently more resistant to shrinkage and dimple formation. Since pressing defects in compacts result from the configurational constitution of voids in the powder before pressing, regardless of interstitial or intragranular in nature, hollow interiors and dimples are candidate features expected to affect the size and distribution of pressing defects in dry-pressed green bodies, which will be partly passed on to their sintered state. As we will show in the sections below, that presumption has turned out to be unsubstantiated.

2.2. Powder Partitioning

Figure 2 shows the density and cumulative particle size distributions of both unsieved 3Y_Control and 5Y_Control (black lines), overlaid onto the distributions of the partitioned fractions resulting from the sieving procedure. The distributions for xY_11 and

xY_20 (see Table 4 and 5 for group labels) are shown as resulting from the Lens R3 measurement, which has a focal length of 100 mm able to differentiate particles in a range from 0.9 to 175 μm . All other shown curves including the mixtures are from the R5 Lens, which has a focal length of 500 mm and can distinguish particles in the range from 4.5 to 875 μm . Both lenses detect particles from a size of 0.5 μm , whereas all particle sizes below the specified measuring range are combined into one size class. In fact, we observed that the R3 lens tends to underestimate particle sizes at the right-end tail of the distribution, with the opposite happening with the R5 lens (see Supporting Information). Because our partitioning is cut at 11 μm (smallest mesh size), readings of submicrometric particles lose importance in favor of accuracy in larger particle sizes ($>100 \mu\text{m}$): there is where the marked difference between the 3YSZ and 5YSZ powders lies. Dimensional reference values are listed in Table 1. It becomes evident that powder partitioning successfully narrowed the size width of the distributions as compared to the control powders, logically shifting the distributions along the size axis. Combined with Figure 2, inspection of Figure 3 allows one to visualize the resulting size distributions of the partitioned fractions of the “single-fraction” xY_11, xY_20, and xY_50 powders after the sieving process; they are not truly discrete “unimodal” since they still have a size distribution.

The rationale for creating “single-fraction” granulate size powders for mechanical testing (xY_20 and xY_50) was to homogenize the interparticle spacing thus inducing a lower packing density by increasing the probability of unfilled interparticle interstices. Models and experiments attest to the inefficiency of mono-sized spheres in increasing packing density, with limits of approx. 0.64 for random dense packed (poured plus tapped) and 0.57–0.61 for loose random packed (only poured) systems.^[17–19] Because these are narrower distributions shifted

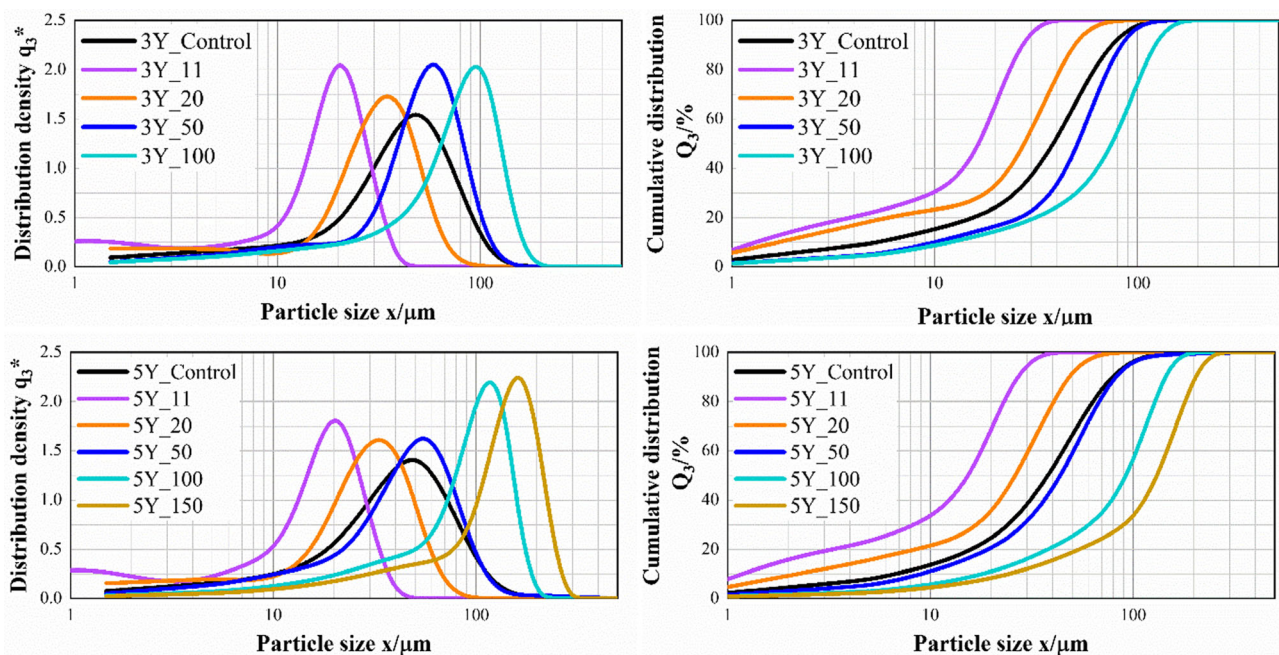


Figure 2. Distribution density and cumulative distributions of the control 3YSZ (upper row) and 5YSZ (lower row) Tosoh powders and of corresponding partitioned fractions (100 mg samples). Partitions xY_11 and xY_20 are from the R3 lens.

Table 1. Dimensional reference values (*d*) of the particle size distributions of the fractions and experimental mixtures, measured whether with the lens R3 or the lens R5. All measurements in μm .

	3YSZ Fractions/Mixtures					5YSZ Fractions/Mixture					
	3Y_11 (R3)	3Y_20 (R3)	3Y_50 (R3)	3Y_100 (R5)	3Y_150	5Y_11 (R3)	5Y_20 (R3)	5Y_50 (R3)	5Y_100 (R5)	5Y_150 (R5)	
$d_{10.3}$	1.32 ± 0.02	1.49 ± 0.04	1.79 ± 0.08	12.12 ± 0.23	–	1.19 ± 0.08	1.37 ± 0.02	1.91 ± 0.19	18.20 ± 0.57	24.57 ± 0.90	–
$d_{50.3}$	16.55 ± 0.18	23.79 ± 0.62	34.00 ± 0.93	75.26 ± 2.05	–	15.44 ± 0.58	21.78 ± 0.24	34.42 ± 1.92	92.71 ± 1.61	132.03 ± 1.59	–
$d_{90.3}$	27.21 ± 0.49	44.94 ± 0.64	59.88 ± 0.48	121.58 ± 1.88	–	27.11 ± 0.55	42.41 ± 1.06	65.53 ± 2.22	143.70 ± 2.00	203.61 ± 2.17	–
	Control (R5)	3Y_20 (R5)	3Y_50 (R5)	3Y_20 + 50 (R5)	3Y_11 + 100 (R5)	Control (R5)	5Y_20 (R5)	5Y_50 (R5)	5Y_20 + 50 (R5)	5Y_20 + 100 (R5)	5Y_11 + 150 (R5)
$d_{10.3}$	5.34 ± 0.62	2.75 ± 0.09	10.17 ± 0.46	6.18 ± 0.90	11.41 ± 0.16	6.78 ± 0.25	3.23 ± 0.10	9.12 ± 1.05	5.48 ± 0.68	10.24 ± 1.24	9.75 ± 0.14
$d_{50.3}$	38.78 ± 2.19	27.82 ± 0.35	50.95 ± 1.76	41.66 ± 1.39	39.00 ± 15.82	38.22 ± 0.93	26.34 ± 0.22	43.97 ± 2.68	35.2 ± 1.49	57.11 ± 5.22	21.6 ± 0.24
$d_{90.3}$	74.67 ± 3.38	49.07 ± 1.19	83.55 ± 1.95	75.84 ± 2.90	123.73 ± 5.50	79.42 ± 2.79	48.53 ± 0.49	82.36 ± 3.15	70.28 ± 2.38	124.23 ± 3.18	164.21 ± 2.77

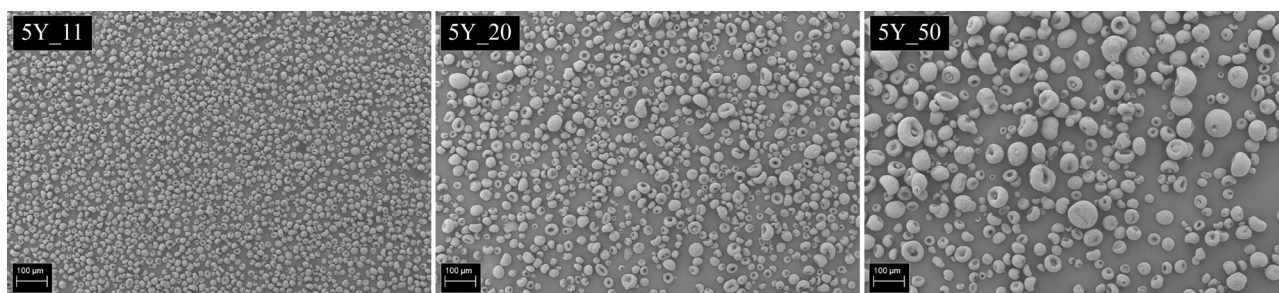


Figure 3. Scanning electron microscopy images of the “unimodal” fractions 5Y_11 (left hand-side), 5Y_20 (middle), and 5Y_50 (right hand-side) after sieving.

along the particle-size axis, differences in the size scale of interstice voids were expected to reflect on the size effect on strength.

Compounding of mixtures was intended to create packing configurations akin to bimodal systems, which benefit from smaller particles filling in interstices between larger particles.^[13] The particle distributions for the experimental mixtures are shown in **Figure 4**. The mixtures $xY_{20} + 50$ do not include the extremes of control powders for direct comparison, while being of interest for comparison with the corresponding single-fraction powders, too; $xY_{20} + 50$ maintained the Gaussian shape once the fractions xY_{20} and xY_{50} make up the bulk of the control powders, thus only eliminating the very small and very large particle fractions. A more marked effect resulted for $5Y_{20} + 50$, which gets slightly shifted left due to the higher amount of the $_{100}$ fraction (≈ 15 wt% in $5Y_{Control}$, vs. ≈ 0.6 wt% in $3Y_{Control}$), and the ≈ 0.6 wt% of the $_{150}$ fraction in $5Y_{Control}$, which is completely absent in $3Y_{Control}$.

Further increasing the efficiency of bimodal configurations is achieved by continuously decreasing the size of the finer

particles in relation to the size of the coarser ones.^[20] The mixtures $3Y_{11} + 100$ and $5Y_{11} + 150$ (and less markedly $5Y_{20} + 100$) show features of bimodal distributions, designed here with the purpose of creating large interparticle spacings that could be filled with finer particles while varying the particle size ratio. The used fraction ratio 25:75 wt% of fine-to-coarse particles for $3Y_{11} + 100$ and $5Y_{20} + 100$ attempted to create a configuration close to modeled ideal bimodal packings.^[20,21] In fact, experiments on metallic and ceramic powders of varying size fractions have confirmed this to be the ideal volume fraction in bimodal size distributions (75–80 vol% of coarser particles and 20–25 vol% of finer particles) as far as defect density is concerned.^[12,17,22–24] In our mixtures, the weight-to-volume transformation suffers from the fact that the real density of the individual granules is unknown due to variations of the hollow interior and thickness of the shell, but assuming density equivalence, our 25:75 wt% should translate roughly into 25:75 vol%. The 65:35 wt% fraction used in $5Y_{11} + 150$ was produced based on the scarcity of these fractions after sieving, and just as for the $3Y_{11} + 100$

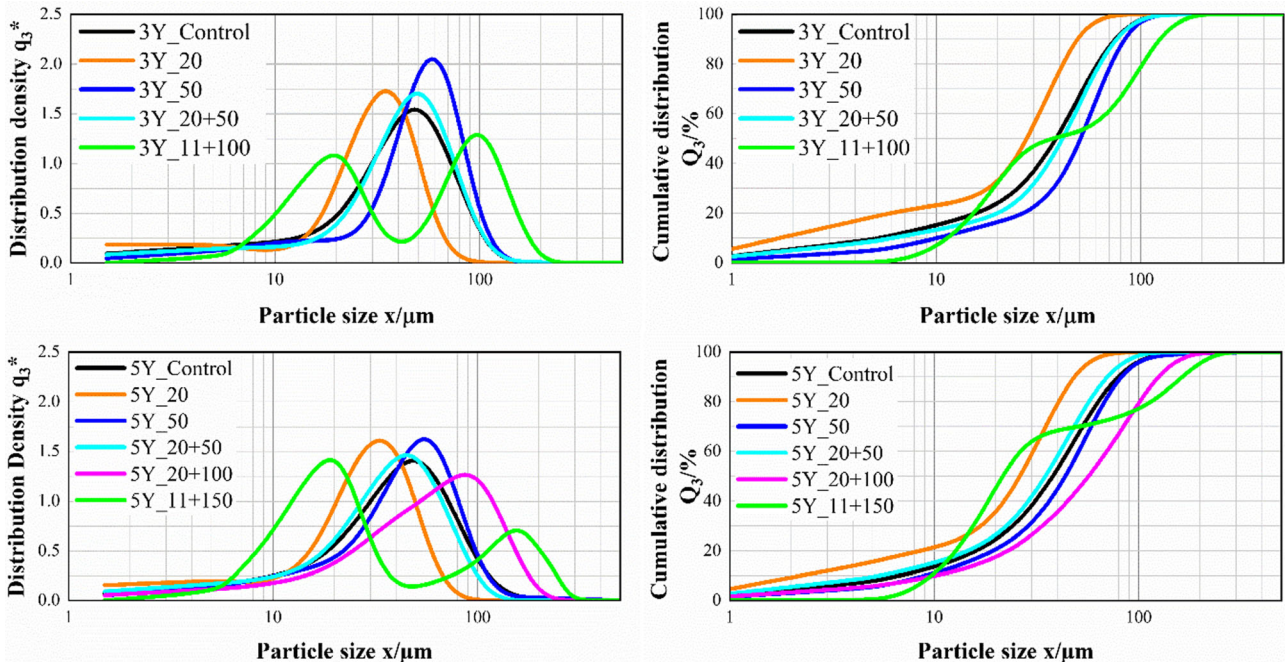


Figure 4. Distribution density and cumulative distributions of the control 3YSZ (upper row) and 5YSZ (lower row) Tosoh powders and of the experimental mixtures (100 mg samples). Only partition xY_20 is from the R3 lens.

fraction, only yielded discs of 0.8 mm in thickness for mechanical evaluation.

Following theory, which predicts that lowering the void density results from broadening the size distribution in continuous particle systems, makes of the control powders the most promising configuration across multiple length scales, since at every given size interval there are finer particles to fill the voids between coarser ones. That assumption gets debunked here in respect to defect size distribution and strength, where specific mixtures have shown to increase the reliability of strength significantly. Of course, idealizations here can be misleading by evoking theories of particles arrangement and spherical packing density, unimodal, bimodal, or continuous distributions. That was only the starting point to design our experimental powder mixtures. Furthermore, one must be aware that our specimens were produced by loose dense packing, not by dense packing that results from tapping the molds to increase particle accommodation. Thus, the packing configuration is that of merely pouring, which can incorporate other voids apart from the interstices formed between particles in a densely packed system. This here is a worst-case scenario when it comes to powder packing.

2.3. Multiscale Fracture Toughness

Table 2 summarizes the fracture toughness values obtained from the “macro” tests for the experimental powders and representative values from “micro” tests for the control powders. Cross-comparisons are contingent on several aspects: for one, 3YSZ is known to exhibit toughening by transformation shielding arising when the metastable tetragonal (*t*) phase reverses into

the stable monoclinic (*m*) allotrope triggered by the high stresses at the crack tip. Added to these dilatational stresses, further toughening ensues by crack deflection and elastic bridging, which can take place in polycrystalline ceramics.^[25–27] These usually scale up with the size of the microstructure^[28] and the path length ahead of the crack tip along which the shielding zone is allowed to develop.^[29] While in 3YSZ these mechanisms are moderated by the small grain size ($\approx 0.2\text{--}0.4\ \mu\text{m}$) and the $\approx 70\ \text{vol}\%$ of the transformable *t*-phase (from which only $\approx 2\text{--}3\ \text{vol}\%$ actually transforms^[30,31]), the microstructure of 5YSZ is dominated by approx. 65 vol% of the low-tetragonality nontransformable Y_2O_3 -rich *t*-phase^[32] that grows into larger grains ($\approx 1\ \mu\text{m}$) during sintering (see Supporting Information for SEMs of the microstructure). The size of the specimen and the unnotched ligament in the μ -cantilevers leave little room for crack face interactions such as elastic bridging to occur in large scale. Due to its much smaller grain size, starting of crack deflection and bridging is already visible in the μ -cantilevers of 3Y_Control during fracture events (see inset in **Figure 5a** and videos of the fracture tests made available in the Supplementary materials). The values of $\mu\text{-}K_{I1}$ as transformed from the *J*-Integral by $K_{I1} = \sqrt{J_1 E / (1 - \nu^2)}$ —which accounts for nonlinearities in the load–displacement curves (be that plasticity or nonlinear elasticity) that also arise in brittle materials in that size scale—were found in remarkable agreement with those of “macro” $K_{I,c}$ -values and only short of about $0.25\ \text{MPa}\sqrt{\text{m}}$. That further gain in toughness can be measured using the CNB method as it allows for several hundreds of microns of stable of crack extension during the test, where microstructure-controlled bridging mechanisms are allowed to evolve and

Table 2. Obtained values of fracture toughness using “macro” tests (CNB) and “micro” cantilevers. $K_{I,c}$ are values calculated using linear-elastic fracture mechanics, while J_I and K_{JI} are obtained using elastic–plastic fracture mechanics principles. Subscript “0” refers to crack initiation toughness, and “max” to the maximum value of the R-curve.

Mixtures of the partitioned fractions	3YSZ			5YSZ	
	$K_{I,c}$ CNB [MPa√m]	μ-cantilever	μ-cantilever	$K_{I,c}$ CNB [MPa√m]	μ-cantilever
		$J_{I,0}$ [J m ⁻²] $K_{JI,0}$ [MPa√m]	$J_{I,max}$ [J m ⁻²] $K_{JI,max}$ [MPa√m]		$J_{I,c}$ [J m ⁻²] $K_{JI,c}$ [MPa√m]
Label xY_Control	4.26 ± 0.07	Test_1: $J_{I,0}$ = 51.0 $K_{JI,0}$ = 2.55 Test_2: $J_{I,0}$ = 29.0 $K_{JI,0}$ = 1.60	Test_1: $J_{I,max}$ = 81.9 $K_{JI,max}$ = 3.99 Test_2: $J_{I,max}$ = 64.1 $K_{JI,max}$ = 3.21	2.52 ± 0.08	Test_1: $J_{I,c}$ = 44.2 $K_{JI,c}$ = 2.25 Test_2: $J_{I,c}$ = 43.9 $K_{JI,c}$ = 2.20
Label xY_20	4.18 ± 0.06	–	–	2.51 ± 0.09	–
Label xY_50	4.19 ± 0.06	–	–	2.29 ± 0.09	–
Label xY_20 + 50	4.22 ± 0.10	–	–	2.54 ± 0.05	–
Label 3Y_11 + 100	–	–	–	–	–
Label 5Y_20 + 100	–	–	–	2.56 ± 0.05	–
Label 5Y_11 + 150	–	–	–	–	–

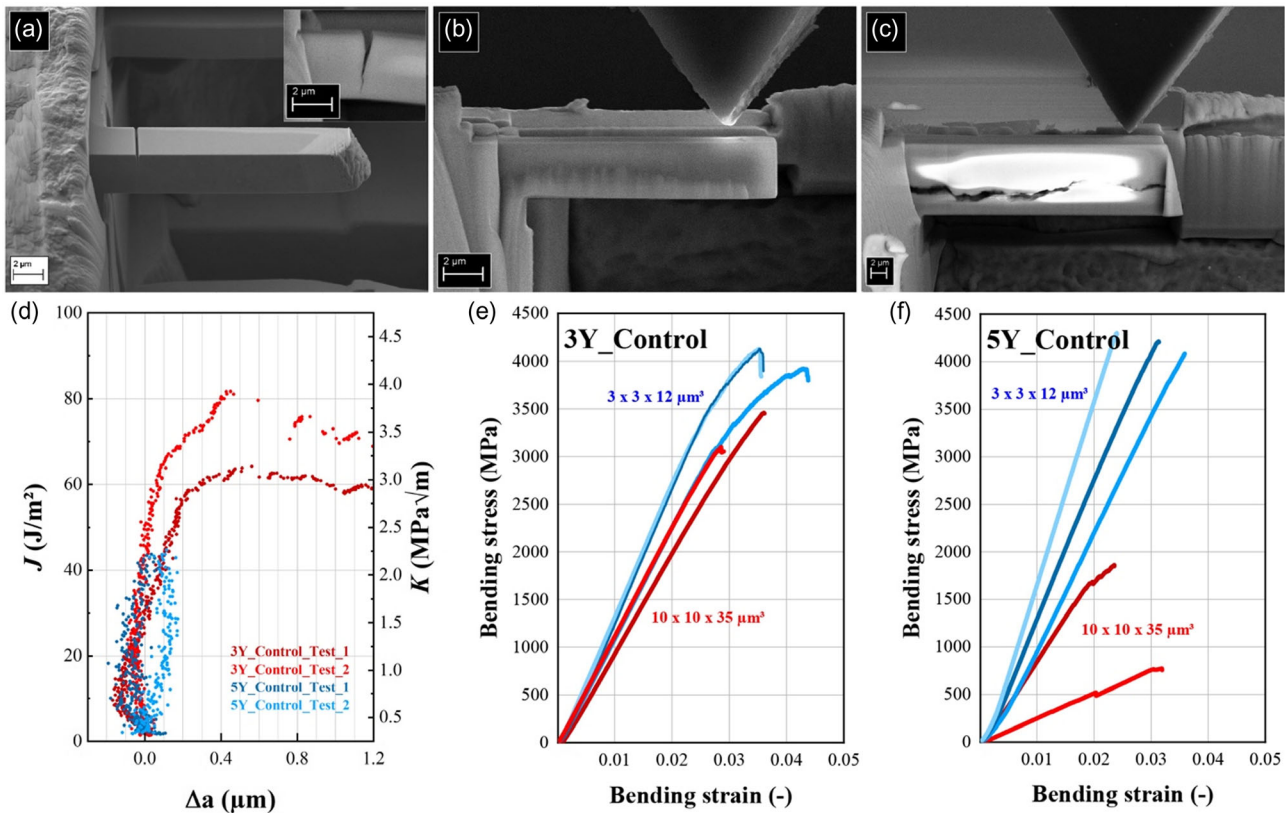


Figure 5. First row: a) SEM image of a FIB-notched μ-cantilever beam of $3 \times 3 \times 12 \mu\text{m}^3$ used for the measurement of “micro” fracture toughness and R-curve. Inset shows the crack growth tracked using the CSM approach. b) SEM image of in situ strength testing in a μ-cantilever with dimensions $3 \times 3 \times 12 \mu\text{m}^3$ of the 3Y_Control material. c) A 5Y_Control μ-cantilever with dimensions $10 \times 10 \times 35 \mu\text{m}^3$ showing a preexisting subsurface defect running along the long axis of the specimen (perpendicular to the pressing direction), which was incorporated into the beam (this specimen is the showing the lowest strength). Second row: d) Dynamic J - and K -values during crack growth of notched specimens; 3Y_Control shows a marked R-curve as opposed to 5Y_Control. e,f) stress vs. strain curves of the μ-cantilever specimens (blue $3 \times 3 \times 12 \mu\text{m}^3$, red $10 \times 10 \times 35 \mu\text{m}^3$). Note the change in compliance for the small 3Y specimens due to R-curve effect of the tetragonal grains. Note the low strength of the larger specimens for the 5Y material due to preexisting defects.

mature into a stable bridging zone. For that reason, values of $K_{I,c}$ obtained using CNB-tests are so-called “long-crack” fracture toughness, which sit farther along the plateau of the R-curve.^[33] The contribution of elastic bridging/deflection to the total shielding stress appears therefore to be comparable in both materials, while transformation toughening provides for as much as $\approx 1.5 \text{ MPa}\sqrt{\text{m}}$ in 3Y_Control. Our $K_{I,c}$ -values found using the CNB method are within the range for 3YSZ and 5YSZ measured by reliable tests elsewhere.^[32,34]

While the $J, K, \Delta a$ curves in Figure 5d reveal that unstable crack growth ensues in 5Y_Control at $J_{I,c}, K_{I,c} \geq J_{I,c}, K_{I,c}$ characterizing a flat-R-curve material, stable crack growth starts at an initiation toughness of $K_{J_I,0}$ of $1.60 \text{ MPa}\sqrt{\text{m}}$ in one specimen and $2.55 \text{ MPa}\sqrt{\text{m}}$ in the other specimen of 3Y_Control. The R-curve in 3Y_Control grows steeply for the first $0.3\text{--}0.4 \mu\text{m}$ —the length of one to two grains—to stabilize thereafter, reaching a plateau $K_{J_I,max}$ at $3.20 \text{ MPa}\sqrt{\text{m}}$ in the one specimen and $3.99 \text{ MPa}\sqrt{\text{m}}$ in the other. Interestingly, when calculated using linear-elastic solutions, all 4 specimens yielded a $K_{I,c}$ of $\approx 2.0 \pm 0.1 \text{ MPa}\sqrt{\text{m}}$, suggesting that nonlinearities were mainly related to crack growth, as opposed to plasticity phenomena such as blunting and tearing common in metallic alloys.

Concerning the fracture toughness of the powder mixtures as measured only using the “macro” CNB-test, no important differences in $K_{I,c}$ -values were detected among the experimental groups, which were all comparable to the respective control groups (see Table 2). This fact supports microstructural equivalence and sintering behavior regardless of the granulate size distribution used. Any variations in defect size distributions would not be expected to be detected using fracture toughness methods and will mainly show up in the purview of the distribution of strength. In turn, seizing on $K_{I,c}$ -values supplies the missing parameter for the calculation of the critical defect size (a_c) distributions from the strength distributions, as will be described in the sections below.

2.4. Multiscale Size Effect on Strength

All relevant parameters rendered by the Weibull statistical treatment of our ≈ 1300 strength tests are listed in Table 3 for each experimental group and testing configuration. Both size and scatter of defects will, respectively, determine the characteristic strength σ_0 and the Weibull modulus m in each specific set of samples. Unfortunately, that says little about how each small cohort defect distribution fits into a broad-scale parent defect population, nor if the latter behaves as a Weibull distribution at all. While practical sample sizes recommended in standards cannot distinguish from similar distributions, the testing for the size effect on strength can infer on the Weibull compliance across several length scales. The varying of specimen size and test configuration alters the effective volume (V_{eff}) to the effect of sampling different cohorts (intervals) of defect sizes within the parent distribution, affecting the obtained strength values correspondingly^[35]

$$P_F(\sigma_r, V_{\text{eff}}) = 1 - \exp\left[-\frac{V_{\text{eff}}}{V_0} \left(\frac{\sigma_r}{\sigma_0}\right)^m\right] \quad (1)$$

where σ_r is a reference tensile stress. Depending on where the critical defects are located, V_0 and V_{eff} can be substituted by S_0 and effective surface S_{eff} . Here, we will first evaluate V_{eff} , which is a function of m in inhomogeneous stress fields,^[36] calculated for the B3B specimens in the two different thicknesses (0.8 and 2.0 mm), following

$$V_{\text{eff},B3B}(m) = V_{\text{sp}} \exp\left[\nu_0 + \nu_1 \frac{m-1}{m+1} + \nu_2 \ln m + \nu_3 m^4 + \nu_4/m\right] \quad (2)$$

with V_{sp} being the total volume of the specimen, and $\nu_{0, \dots, 4}$ fitting constants. Interactive calculations of V_{eff} for B3B specimens are made available in the Supporting Information of Staudacher et al.^[36] For 4-point bending (4PB) in a $1/4$ span geometry, and 3-point bending (3PB), V_{eff} are obtained by^[37]

$$V_{\text{eff},4PB}(m) = \frac{LBW(m+2)}{4(m+1)^2} \quad (3)$$

$$V_{\text{eff},3PB}(m) = \frac{LBW}{2(m+1)^2} \quad (4)$$

with L , B , and W being the support span length, the width, and the height of the specimen, respectively. For a cantilever specimen, V_{eff} is given in ref. [38] as

$$V_{\text{eff},\mu\text{-cant}}(m) = \frac{LBW}{4(m+1)} \quad (5)$$

The corresponding mean values for V_{eff} for each specimen size and test configuration are included in Table 3.

Based on the collection of parameters given in Table 3, one telltale pattern already stands out suggesting the nonconformity of the strength distributions to a multiscale Weibull behavior. Namely, the Weibull modulus is always higher (consistently 2 digit) for the smallest of the “macro” V_{eff} (i.e., B3B_0.8 mm specimens); and at least twofold, up to fivefold, higher than that of the Weibull modulus of the largest “macro” V_{eff} (i.e. 4PB_40 span specimens). This was systematic throughout the experimental groups—for both materials. The requisite for a “Weibull material”, i.e., that the Weibull modulus of two different specimen sizes, say “a” and “b”, be independent on the applied stress (strength) and effective volume,^[39,40] is violated, i.e., the condition

$$V_{\text{eff},a} \sigma_a^m = V_{\text{eff},b} \sigma_b^m \quad (6)$$

does not hold. Now, if $a < b$, this is especially the case for $a = \text{B3B}_0.8 \text{ mm}$ and $b > \text{B3B}_2.0 \text{ mm}$. When $b = \text{B3B}_2.0 \text{ mm}$, the requisite Equation (6) is true for all groups, but it breaks down for higher effective volumes (specimen sizes). The double-logarithmic plots of strength vs V_{eff} in Figure 6 illustrate that relationship across all evaluated length scales, more specifically, over five orders of magnitude (from $\approx 2 \mu\text{m}^3$ up to $\approx 20 \text{ mm}^3$ —note that V_{eff} is highly dependent on m). For the control groups, the inclusion of the results of the μ -cantilevers $3 \times 3 \times 12 \mu\text{m}^3$ (see Figure 6, first plot in each row) expand the scales to stresses $> 4000 \text{ MPa}$ and $V_{\text{eff}} < 10^{-9} \text{ mm}^3$.

Table 3. Summary of the Weibull parameters and effective volumes (V_{eff}) of the multiscale strength tests. X is the number of specimens. Numbers formatted in bold are double-digit Weibull moduli.

Experimental group	X	σ_0 [MPa]	σ (90% C.I.) [MPa]	m	m (90% C.I.)	V_{eff} [mm ³]	V_{eff} (90% C.I.) [mm ³]
3Y_Control_B3B _{0.8 mm}	30	1680.6	1640.0–1722.8	13.0	10.2–16.6	0.0099	0.0176–0.0057
3Y_Control_B3B _{2.0 mm}	30	1221.4	1176.1–1269.1	8.4	6.6–10.8	0.2275	0.4075–0.1277
3Y_Control_4PB Span 40	34	767.7	735.8–801.2	7.0	5.6–8.9	16.3740	20.31–12.94
3Y_Control_4PB Span 20	33	882.9	836.1–932.7	5.6	4.4–7.0	10.2031	12.83–8.22
3Y_Control_3PB Span 20	30	837.9	777.5–903.7	4.3	3.3–5.5	4.1875	6.36–2.78
3Y_Control_μ-Cantilever	3	4101.5	4041.2–4259.4	30.5^{a)}	24.4 – 40.4	7.14×10^{-10}	$8.85 \times 10^{-10} - 5.43 \times 10^{-10}$
3Y_20_B3B _{0.8 mm}	32	1656.3	1634.9–1678.2	23.7	18.8–30.0	0.0027	0.0044–0.0016
3Y_20_B3B _{2.0 mm}	30	1213.6	1157.2–1273.4	6.7	5.3–8.6	0.3918	0.7086–0.2151
3Y_20_4PB Span 40	34	733.8	694.8–775.4	5.5	4.4–6.9	20.6364	25.51–16.57
3Y_20_4PB Span 20	34	824.4	794.8–855.3	8.2	6.5–6.9	7.0456	8.83–5.63
3Y_20_3PB Span 20	29	885.2	805.3–974.2	3.4	2.7–4.4	6.0157	8.50–3.99
3Y_50_B3B _{0.8 mm}	30	1605.9	1557.5–1656.3	10.4	8.2–13.3	0.0169	0.0306–0.0095
3Y_50_B3B _{2.0 mm}	30	1192.8	1136.2–1252.8	6.6	5.2–8.4	0.4076	0.7433–0.2275
3Y_50_4PB Span 40	38	687.8	663.5–713.3	7.8	6.3–9.7	14.7503	18.15–11.91
3Y_50_4PB Span 20	35	757.9	725.9–791.5	6.8	5.5–8.6	8.4576	10.37–6.72
3Y_50_3PB Span 20	42	883.8	846.2–923.4	6.1	5.0–7.5	2.3322	3.26–1.62
3Y_20 + 50_B3B _{0.8 mm}	30	1687.6	1646.3–1730.3	12.9	10.1–16.5	0.0100	0.0179–0.0058
3Y_20 + 50_B3B _{2.0 mm}	30	1195.0	1142.6–1250.5	7.1	5.6–9.1	0.3327	0.6060–0.1848
3Y_20 + 50_4PB Span 40	34	676.1	650.2–703.3	7.6	6.1–9.6	15.0838	18.67–11.99
3Y_20 + 50_4PB Span 20	33	753.0	716.8–791.5	6.2	4.9–7.8	9.3525	11.71–7.48
3Y_20 + 50_3PB Span 20	33	849.7	808.3–893.6	6.1	4.8–7.7	2.3231	3.48–1.54
3Y_11 + 100_B3B _{0.8 mm}	30	1712.8	1677.3–1749.4	15.3	12.0–19.5	0.0068	0.0119–0.0040
5Y_Control_B3B _{0.8 mm}	31	1034.7	1011.3–1058.8	13.8	10.8–17.5	0.0085	0.0150–0.0050
5Y_Control_B3B _{2.0 mm}	29	811.1	782.4–841.2	9.0	7.0–11.6	0.1893	0.3433–0.1070
5Y_Control_4PB Span 40	30	436.1	413.4–460.4	6.0	4.7–7.6	19.0390	24.04–15.13
5Y_Control_4PB Span 20	28	431.9	396.2–471.3	3.8	3.0–5.0	14.8707	18.46–11.48
5Y_Control_3PB_Span 20	27	459.8	435.1–486.2	6.1	4.7–7.9	2.3323	3.61–1.48
5Y_Control_μ-Cantilever	3	4242.2	4174.0–4421.1	27.9^{a)}	22.3–37	7.78×10^{-10}	$9.66 \times 10^{-10} - 5.92 \times 10^{-10}$
5Y_20_B3B _{0.8 mm}	31	1000.9	979.2–1023.3	14.3	11.3–18.2	0.0078	0.0134–0.0046
5Y_20_B3B _{2.0 mm}	30	849.3	821.1–878.8	9.5	7.4–12.1	0.1663	0.2994–0.0965
5Y_20_4PB Span 40	28	383.8	360.2–409.3	5.2	4.1–6.7	21.9332	27.46–17.18
5Y_20_4PB Span 20	27	425.0	399.5–452.5	5.4	4.2–7.1	10.5778	13.42–8.12
5Y_50_B3B _{0.8 mm}	30	991.4	971.9–1011.5	16.1	12.6–20.5	0.0061	0.0106–0.0036
5Y_50_B3B _{2.0 mm}	30	834.0	801.0–868.7	7.9	6.2–10.1	0.2557	0.4627–0.1447
5Y_50_4PB Span 40	22	363.3	342.5–385.8	6.4	4.8–8.5	17.8054	23.46–13.50
5Y_50_4PB Span 20	22	414.4	394.7–435.4	7.7	5.8–10.3	7.4377	9.79–5.59
5Y_20 + 50_B3B _{0.8 mm}	30	954.3	943.5–965.2	28.2	22.1–36	0.0018	0.0030–0.0011
5Y_20 + 50_B3B _{2.0 mm}	31	829.4	807.4–11.7	11.7	9.2–14.9	0.1043	0.1793–0.0617
5Y_20 + 50_4PB Span 40	21	334.6	308.7–363.3	4.8	3.6–6.4	23.6076	30.90–17.91
5Y_20 + 50_4PB Span 20	21	349.2	324.5–376.2	5.2	3.9–7.1	10.9375	14.34–8.09
5Y_20 + 100_B3B _{0.8 mm}	31	924.2	897.5–951.9	10.7	8.4–13.6	0.0160	0.0292–0.0091
5Y_20 + 100_B3B _{2.0 mm}	30	778.3	745.5–812.9	7.4	5.8–9.5	0.3032	0.5535–0.1685
5Y_20 + 100_4PB Span 40	23	324.4	304.3–346.1	5.7	4.3–7.6	20.0292	26.18–15.15
5Y_20 + 100_4PB Span 20	23	382.0	357.3–408.8	5.5	4.2–7.3	10.3640	13.38–7.88
5Y_11 + 150_B3B _{0.8 mm}	30	987.9	966.8–1009.7	14.8	11.6–18.9	0.0072	0.0126–0.0042

^{a)}fitted to and corrected by $X = 3$.

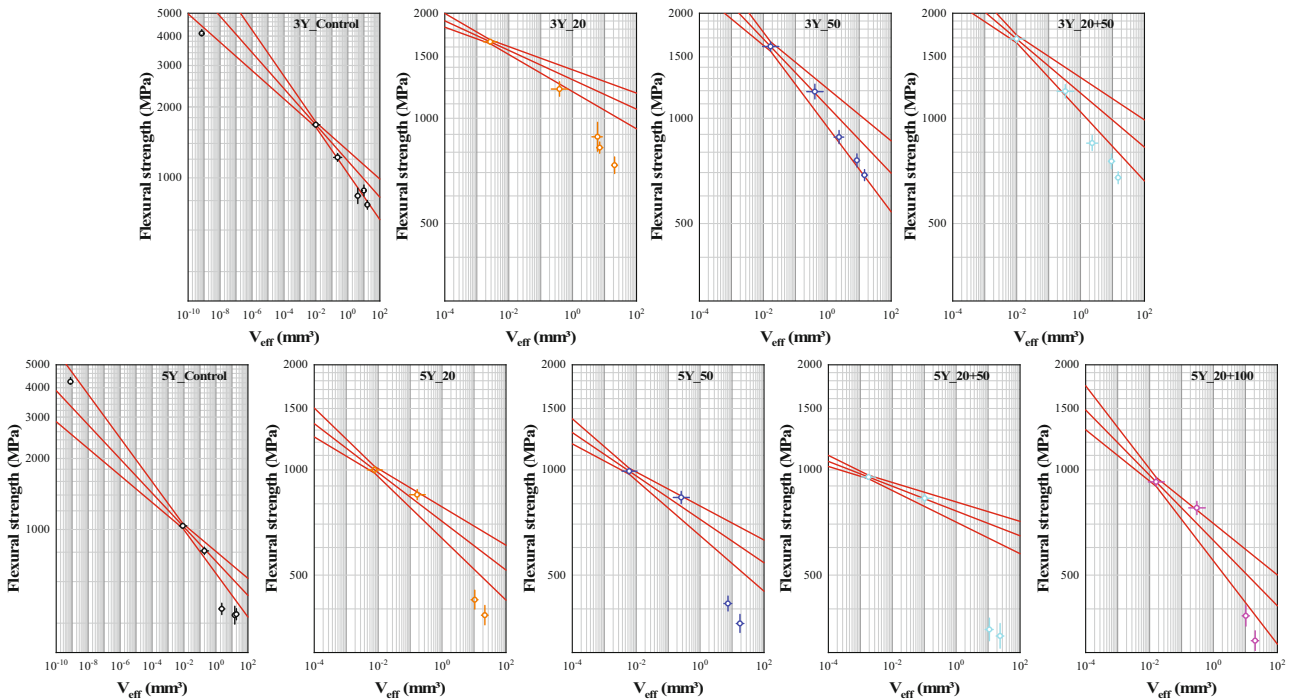


Figure 6. Weibull strength size-effect plots (flexural strength vs. effective volume, V_{eff}) for the 3Y_ (upper row) and 5Y_ (lower row) control and mixtures. Data points relate to the specific testing geometry and specimen size. Error bars are the 90% CIs for strength and V_{eff} . The central lines are the Weibull estimation when downscaling or upscaling from the B3B_0.8 mm specimen. Data points falling outside the 90% confidence intervals (upper and lower lines) fail to comply with the Weibull behavior.

In these plots, the center red lines are the Weibull strength predictions toward smaller (downscaling) and larger (upscaling) effective volumes based on the strength distribution of the B3B_0.8 mm specimen. The slope of this line is the negative reciprocal of the Weibull modulus ($-1/m$) (the outer bands are the 90% CIs), which will largely establish the compliance (or noncompliance) of the other datasets (other volumes) to the Weibull behavior. In other words, the obeying of a multiscale Weibull behavior requires that the data points for all specimen sizes align with the center line, or at least fall within the 90% confidence bounds.^[39,41,42] The fact that the data points for the B3B_2.0 mm specimen always fit well to the Weibull prediction, and the others with larger V_{eff} do not, suggests that there is a transitional volume between ≈ 0.2 and $\approx 2 \text{ mm}^3$, within which a different defect population of larger size starts to become dominant and trigger fracture in the “macro” bending beams. These larger defects might just be too large and appear much less frequent that they are missed to be sampled at the one very small volume where the stress is maximum in the B3B specimens. Whether the lower scale defect population remains underlying is not readily accessible, since the defect size is too small to compete with the now larger critical defects. The latter can still behave Weibullian toward higher lengths scales, but the self-similarity to the distribution at lower orders of magnitude is lost.

One notes from Figure 6 that the hitherto statements on the compliance with the Weibull behavior were generalized. In fact, in two occasions, Equation (6) holds in all length scales, namely for the 3Y_Control powder and for the single-fraction 3Y_50. In

both cases, the data points for the “macro” bending beams touch or lie on the lower bound of the uncertainty bands, not because they were shifted to higher strength values relative to the other groups, but mainly as a direct effect of the Weibull modulus of their B3B_0.8 mm specimens. The lowest moduli for that size, 3Y_50 and 5Y_20 + 100 (and both control groups, though less markedly), show the steepest slopes, indicating that the scatter of defect sizes in the smallest scale starts to get wide enough to almost become indistinguishable from an underlying defect population that stretches all the way to shape the strength distribution in the largest scale. In contrast, the highest Weibull moduli, found for 3Y_20 and 5Y_20 + 50 (23.7 and 28.2, respectively), indicate that altering the particle size distribution can actually have an effect on the distribution of pressing defects insofar as the scatter of critical defect sizes in the lowest length scale is concerned. In that length scale, narrowing and homogenizing the interparticle interstice size distribution (and any other void size due to intraparticle hollow space and dimple) can increase the reliability of strength by way of decreasing the scatter in the defect size distribution. Whereas a mixture broadening the granulate size density to include the _50 single fraction contributed to this effect in the 5YSZ powder, a narrower 3Y_20 fraction was more effective in the 3YSZ powder, pointing, perhaps, to some granulate shape effect. The significantly lower Weibull modulus in that length scale for all other experimental powders seems to attest to the negative role of the presence of size fractions of very large granulates. As much as that effect on the smallest size scale is compelling, so is the fact that it failed to reach higher orders of

magnitude (although m for B3B_2.0 mm in 5Y_20 + 50 was also substantially increased). This again suggests that the distribution of defect sizes in larger effective volumes incorporates defects that are not scalable in size from the smallest effective volume when departing from a Weibull distribution. This can be further instantiated by the Weibull strength scaling law in the form of a pooled Weibull representation. By rearranging Equation (6), the strengths of all other specimen sizes can be downscaled (upscaled in the case of the μ -cantilevers) by means of the ratio of effective volumes from a reference specimen size, here the B3B_0.8 mm-thick disc

$$\sigma_{f,x} = \sigma_{f,B3B,0.8} \left(\frac{V_{\text{eff}, B3B,0.8}}{V_{\text{eff},x}} \right)^{1/m_{B3B,0.8}} \quad (7)$$

with the index “ x ” referring to all other specimen sizes; the Weibull modulus is of the B3B_0.8 mm tests. This procedure extrapolates the strengths obtained in specimens of different sizes to a mean V_{eff} of the B3B_0.8 mm dataset, that is, as if they had the same size as the thinnest discs as per a Weibull behavior.^[36,39] That results in the pooled Weibull plots in Figure 7, where the obtained strengths from Equation (7) from all datasets are arranged in one single failure probability. Same colored data-points belong to the same specimen size. The evaluation depicted in Figure 7 is a first iteration of a simplified least-squares pooled evaluation; a more complex procedure considering the V_{eff} of all specimen sizes as a function of the unknown m can be

performed using the procedure given in ref. [36] using Equation (25) and (26) therein.

Noteworthy is the excellent fit of the data-points of 3Y_Control and 3Y_50 onto the straight black line (giving a pooled m -value), a hallmark of a Weibull distribution. 5Y_20 + 100 also behaves similarly. These are the groups that most conformed to the Weibull size-effect prediction in Figure 6 (note that in Figure 6 the strength data are not yet transformed to the smallest volume as per Equation (7)). When the distribution is of the Weibull type across all length scales, the scaling of strength to one single effective volume distributes the data-points of all specimen sizes over the entire range of failure probabilities. Meaning that the colors in the dataset would mix somewhat evenly along the line. That does not happen for a non-Weibull behavior, with the data-points segregating by size (color), that is, smaller volumes (higher strengths) at higher failure probabilities and vice versa. We see a better mixing of the datasets for the Weibull groups (3Y_Control and 3Y_50), though the B3B data-points still dominate the high-strength tail of the distribution, once the 3,4PB specimen border the lower bounds of the Weibull prediction and are responsible for the lower strengths (note the 3Y_Control μ -cantilevers shifting down the failure probability scale, the 5Y_Control ones remaining as the highest values). For the other (non-Weibull) groups, not only this segregation occurs more clear-cut but also the pooled distribution diverges from a straight line with the transition between B3B and 3,4PB datasets forming bulges and steps.

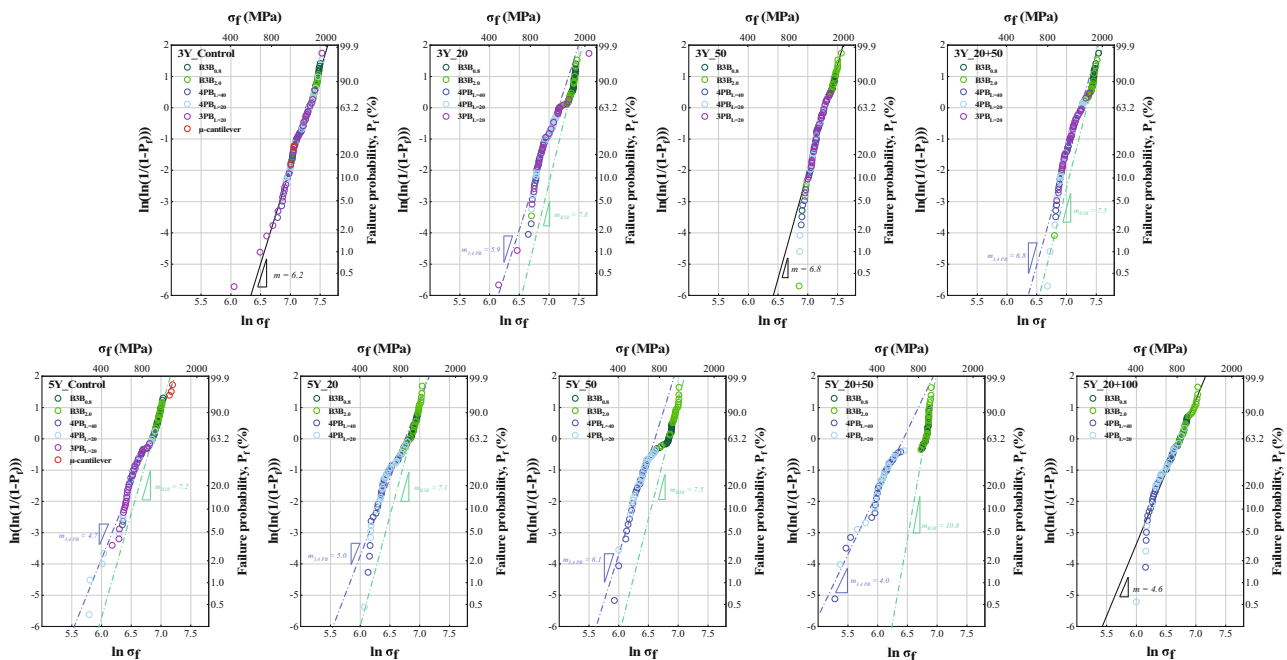


Figure 7. Pooled Weibull plot for each experimental group with the transformed strength data-points for different specimen sizes to the effective volume of the B3B_0.8 mm specimen. Note the better mixture of colors (data-points from different specimen sizes) within the datasets of 3Y_ and a clearer separation in size hierarchy in the 5Y_ material. Note how the only mixtures that followed the Weibull strength-size prediction, namely 3Y_Control and 3Y_50, also are the only ones fitting well the straight-line characteristic of Weibull materials. The small specimens (B3B) of the other groups generally tended to show a much steeper slope (higher Weibull modulus) as the remaining distribution of strengths resulting from the larger specimens (4PB, 3PB). The black line is the MLE fit to all the data for the groups showing Weibull behavior in all length scales (not good fit to the straight line). The blue dashed line is only fitted to the 3,4PB data; the green dashed line is only fitted to the B3B data.

These shapes are symptomatic of the presumed bimodal parent defect population that must yield different Weibull parameters. The superposition of these two distributions is expressed by a probability that failure will be triggered by one or the other population, say “p1” and “p2”

$$P_F = 1 - \exp \left[- \left(\frac{\sigma_f}{\sigma_{0,p1}} \right)^{m_{p1}} - \left(\frac{\sigma_f}{\sigma_{0,p2}} \right)^{m_{p2}} \right] \quad (8)$$

with failure at low probabilities being caused by the population with the lower value of m .^[43] In Figure 7, the fitting of the two populations results in the dashed lines in blue and green, if say $p1 = 3,4PB$ and $p2 = B3B$. The slopes of the green fitting lines in this pooled distribution tend to be steeper (higher moduli, between 7 and 10) than the blue slope at lower failure probabilities and larger volumes (moduli <6). This is, of course, a direct consequence of the Weibull moduli of the single datasets.

Now, a better picture fails to take shape in Figure 6 and 7 if the effective surface (S_{eff}) is evaluated, as far as a Weibull compliance goes (see Supporting Information). In that instance, the Weibull prediction line is shifted farther away from the data-points of the large specimens, and none of the groups now would conform to a Weibull distribution. However, the calculation of the size of the critical defects in those distributions may suggest that defects on the surface of B3B_0.8 mm specimens need not be discarded as possible failure location. It might therefore as well be that as the effective volume passes a certain threshold dimension, only the underlying smaller-sized defects are sampled on the surface, and the two defect populations across multiple length scales is formed by volume defects in 3,4PB specimens and in the surface for B3B specimens, analogously to Equation (8)^[43]

$$P_F = 1 - \exp \left[- \frac{V_{eff,3,4PB}}{V_0} \left(\frac{\sigma_f}{\sigma_{0,V,3,4PB}} \right)^{m_{V,3,4PB}} - \frac{S_{eff,B3B}}{S_0} \left(\frac{\sigma_f}{\sigma_{0,B3B}} \right)^{m_{S,B3B}} \right] \quad (9)$$

Large pressing defects can also form at the surface/subsurface, though less frequently, as coincidentally caught in the two 5Y_Control μ -cantilevers having $10 \times 10 \times 12 \mu\text{m}^3$ (milled side-by-side from a piece of broken 4PB specimen), as shown in Figure 5c,f (due to that and the small sample size of 2, μ -cantilevers of $10 \times 10 \times 35 \mu\text{m}^3$ were not included in the analysis of Figure 6 and 7). Below, in Figure 9, another example of an interconnecting pressing void at the subsurface is shown. Although existent, such large defects might have just occurred too unfrequently, or outside the zone of maximum stress, to have an impact on the strength distributions. As will be demonstrated later, fracture was rarely triggered by defects larger than $50 \mu\text{m}$.

The data-points in Figure 6 relative to the μ -cantilevers must also be interpreted with caution, since only three specimens were used for the estimation of the Weibull modulus, and the correction a per the number of samples^[44] reduced the original value to about half. Considering that the Weibull modulus also enters the calculation of V_{eff} , the position in the abscissa is also liable

to changes. Nevertheless, the observed strength for the μ -cantilevers seems to fit the Weibull predictions extrapolated from a B3B_0.8 mm size quite well, despite the tendency of very small specimen sizes to become incongruent to the predictions of the Weibull theory, which estimates densities of small defects exceeding the actual material volume,^[40] as suggested by the experiments in Ref. [45]. The nature of defects must be of a different nature, simply because the μ -cantilevers are not pressed, but milled out of pressed specimens; the probability of catching a pressing defect in the FIB-milling zone, although realistic (see Figure 5c), is different than the probability distribution of pressing-defect sizes in that specimen.

2.5. Critical Defect Densities: Calculations and Measurements

All samples have been fired to full densification. The sintered densities are specified and explained in the Supporting Information. A clear effect of powder partitioning on the density could not be proven, so that a discussion of microstructure and defect distribution based on the density values does not appear to be meaningful.

The strength datasets are much more useful for that analysis. The radius of the critical defect for each strength value in a dataset can be calculated using the Griffith/Irwin relation by seizing on the “macro”- $K_{I,c}$ values, via

$$a_{c,i} = \frac{1}{\pi} \left(\frac{K_{I,c}}{Y\sigma_{f,i}} \right)^2 \quad (10)$$

where Y is the geometrical correction factor, assumed to $2/\pi$ for penny-shaped defects embedded in the volume.^[35] The sizes of defects for B3B and 3,4PB specimens are given exemplarily for the Control groups in Figure 8a,b against the density $n_c(a_c)$ of critical defect sizes, given by

$$n_c(a_c) = \frac{a_{c,i}}{r-1} \times g(a_{c,i}) \quad (11)$$

where the second term is the relative defect size density function $g(a)$ ^[40]

$$g(a_{c,i}) = \frac{r-1}{V_{eff} a_{c,i}} \ln \frac{2X}{2X-2i+1} \quad (12)$$

with $a_{c,i}$ obtained for each specimen via Equation (10), X is the number of specimens, and r is the exponent in $g(a) = g_0(a/a_0)^{-r}$, which is related to the Weibull modulus m by $r = (m/2) + 1$.^[39] The size (radii) of defects necessary to induce fracture in the B3B_0.8 mm specimens were in the range of 3–8 μm and within 6–20 μm for B3B_2.0 mm specimens. Among the bending beams, the differences in effective volumes were not so significant, and the critical defect size triggering failure were comparable, between 10 and 100 μm (presumably CP-defects and multiple connected IJV-defects). Noteworthy is the matching of defect sizes across length scales for both powders, negating the hypothesized effect related to granulate morphology. Whether granules form dimples or not, the defect sizes and their distribution in YSZ powders seem to remain unchanged.

μ -computer tomography scans were performed in the center of $\approx 1 \text{ mm}^3$ sections of selected B3B_0.8 mm discs precisely to

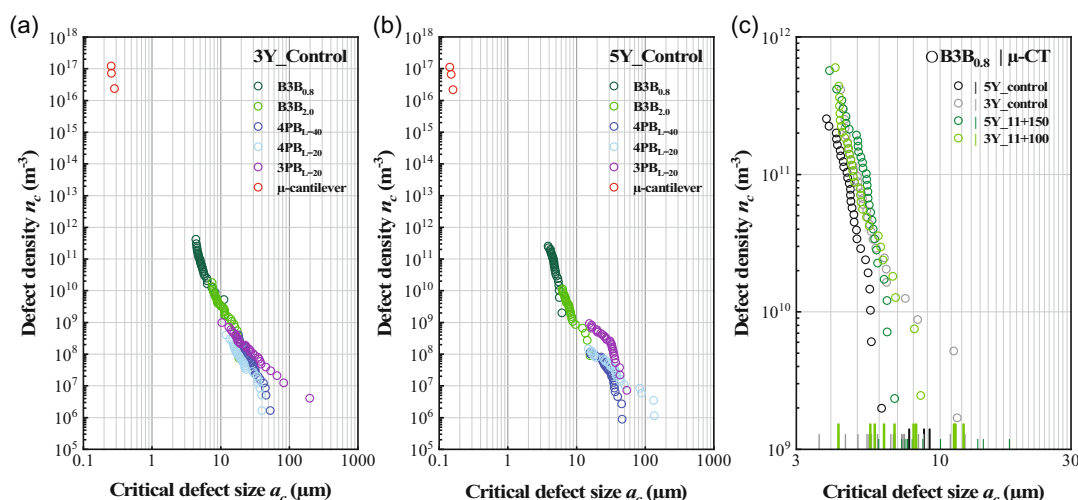


Figure 8. Defect density versus calculated critical defect size for all specimens of the control groups a,b) and for the B3B_{0.8} mm specimens including those of 3Y₁₁ + 100 and 5Y₁₁ + 150 c) overlaid to the radii of defects found by μ-CT (lines on the x-axis).

evaluate if the calculated dimensions of a_c befit a realistic range of pressing defects that are actually found in the specimens. The radii of defects detected by μ-CT are overlaid as dashes onto the x-axis in Figure 8c for each group; the agreement of sizes between measurement and calculation is remarkable, supporting that those defects in the volume could be responsible for the fracture of B3B_{0.8} mm discs. The spatial distribution of these defects can be seen in Figure 9, with no apparent defect concentration or gradients being noticeable. The shape of the defects seems spherical to ellipsoid and could represent the core of IJV-defects between pressed granules. Defects larger than 10 μm, which would mainly be responsible for fracture of the

larger beam specimens, started to appear much less frequently and would probably be sampled in much larger specimen volumes. A list of the volumes and sizes of the defects in Figure 8c and 9 are given in a Table in the Supporting Information. Most remarkably is the matching of the predicted defect density by Equation (11) and (12) with the actual number of defects found within the ≈1 mm³ volume scanned by the μ-CT. Using V_{eff} in Table 3 for the B3B_{0.8} mm specimens, the range of probable defect densities for the “weakest” and “strongest” specimens in the datasets of X specimens yields about 2 and 500 defects per mm³, respectively (see γ-axis in Figure 8). The randomly picked specimens for the μ-CT analysis

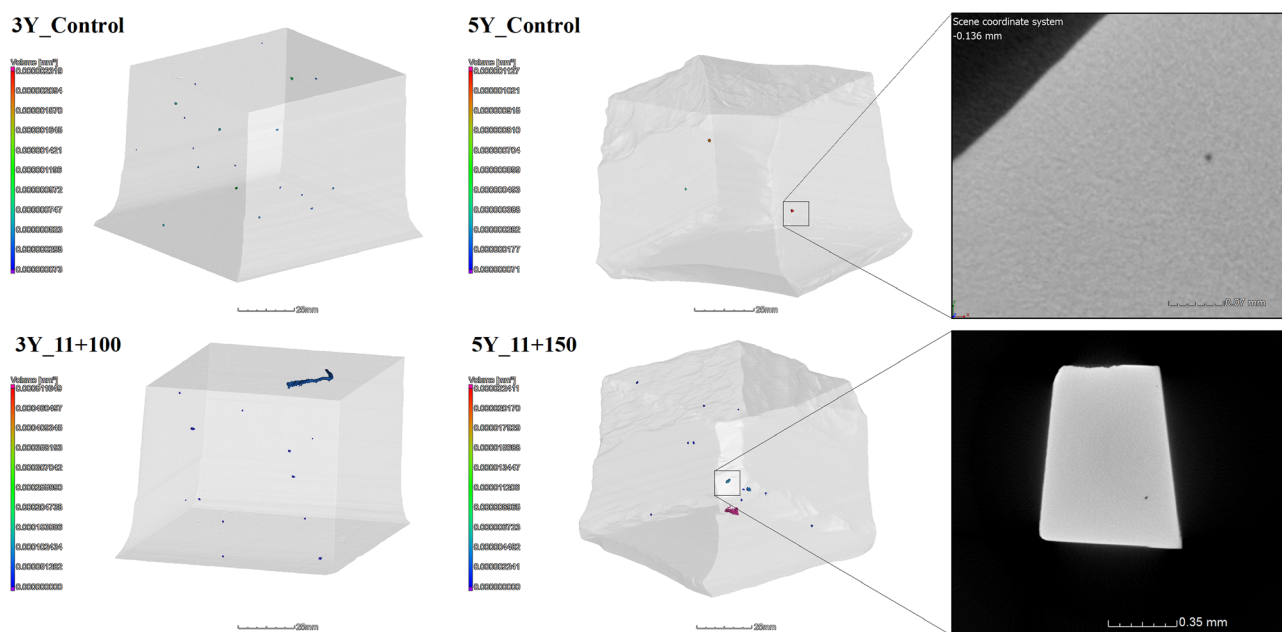


Figure 9. Spatial reconstruction of the ≈1 mm × 1 mm × 0.8 mm samples sectioned out of the center of B3B_{0.8} mm discs. The volume of defects is shown in color coding. In the right-hand side, tomography sections are shown showing the cross-sectional shape of selected defects.

all show defects within that range (closer to the lower bound, between 3 and 19 defects, see Supporting Information), considering that defects of radii $<5\ \mu\text{m}$ have most probably gone undetected due to the limits of the $\mu\text{-CT}$ resolution (such as IP-defects). This agreement between prediction and measurement further supports the use of fracture statistics for analysis of the scatter of strength in ceramic materials.

The size of the critical defects calculated for the $\mu\text{-cantilevers}$ are also plotted in Figure 8a,b. For 3Y_Control, Equation (10) yielded $a_c = 200\text{--}300\ \text{nm}$, which is comparable to the size of single grains. The unexpected high strength of the $\mu\text{-cantilevers}$ of 5Y_Control despite its lower $K_{I,c}$ rendered an even smaller defect size, namely $a_c \approx 150\ \text{nm}$, pointing to defects being activated inside the grains or at grain boundaries/junctions, given that large grains ($0.5\text{--}1\ \mu\text{m}$) end up being too large compared to the size of the specimen to act as individual defects. For such small effective volumes, the prediction to the Weibull behavior also starts to get lost (see Figure 6), reinforcing the idea that defects in that scale diverge from the nature of pressing defects governing the macroscale fracture behavior.

3. Conclusion

Our attempt here to tailor the pressing defect distribution of commercial YSZ spray-dried powders by changing the distribution of the granulate sizes showcases the utility of multiscale strength testing in evaluating the (non)compliance to the Weibull behavior across several length scales, which can be relevant for different applications.

We showed that either in control powders or in powder mixtures, a high Weibull modulus is always achieved for the smallest “macro” test specimen, and low moduli are consistent for large specimen volumes, an indication of different defect populations governing the fracture behavior at small and large scales. “Micro” and “macro” tests tended to follow the Weibull prediction on strength up to an effective volume of about $0.2\ \text{mm}^3$, breaking down for higher volumes up to $20\ \text{mm}^3$. The narrowing of the size distribution of granulates by removing the extreme granulate sizes has shown the potential to increase the strength reliability (Weibull modulus) of 3YSZ and 5YSZ, provided that the effective volume is very small (for small components). Changing the granulate size distribution was ineffective in improving the strength for larger volumes (large components). Both calculated and measured defect sizes agreed well at the smallest evaluated scale. The predicted defect density matched very well the measured defects number in the same specimen volume. The morphology of the granulate before pressing (dimpled or not) did not affect the pressing defect size distribution.

4. Experimental Section

YSZ Feedstocks: Two commercial YSZ feedstocks with wide industrial applications were selected for this study, namely a 3 mol% Y_2O_3 -stabilized zirconia (Zpex, Tosoh, Japan) and a 5 mol% Y_2O_3 -stabilized zirconia (Zpex Smile, Tosoh). These two powders were selected due to their different granulate morphology (see Figure 1), different size distributions (see Figure 2), and different fracture toughness of the densely sintered materials, with the 3YSZ material exhibiting the toughening mechanism of

tetragonal-to-monoclinic phase transformation, whereas this is mainly absent in the 5YSZ material.

The granulates were purchased through an official Tosoh representative in Germany (Krahn Ceramics, Germany) in 1 kg containers and used as delivered.

Powder Partitioning and Analysis: In order to partition the initial 3YSZ and 5YSZ powder distributions into several narrower size distributions and mixtures thereof, a sieving procedure was performed following the guidelines of ASTM C136 standard in a set of sieves of mesh sizes of 250, 200, 150, 100, 50, 20 and 11 μm . Apart from the 11 μm sieve, which had a nylon fabric, all sieves were made of stainless steel. The sieving was performed in the equipment Retsch-model AS 200 basic, using 500 g of the corresponding feedstock powders for 10 min with an amplitude of 50 Hz, with the sieves being cleaned in water in an ultrasonic bath after each sieving round (Figure 10c). The size distribution of powders left in each sieve exhibits a size interval limited approximately by its mesh size and the previous mesh size, but will be here labeled using only the size of the lower limit (see Table 3). The fractions of powder remaining in each sieve were weighted and conserved separately in plastic containers. The resulting weight fraction for each 1 kg of powder is listed in Table 4. The partitions 20 μm and 50 μm were more abundant in both powders, making of most of the weight. Powder 3YSZ yielded no 150 μm partition. Because of their lower fractions, partitions 11, 100, and 150 μm could not be collected to a large enough amount to allow for them to be used as “unimodal” separately. Thus, different mixtures from 3Y_ and 5Y_ were designed according to the amount (weight) of size fraction obtained in the sieving process. For both materials, mixtures containing only 20 or 50 μm were produced, with the remaining fractions used in “bimodal” mixtures, as given in Table 5. Due to the very low amount of the powder fractions 3Y_11, 3Y_100, 5Y_11, and 5Y_150, the mixtures 3Y_11 + 100 and 5Y_11 + 150 could not be produced for the entire range of specimen sizes and were only produced for biaxial flexure in discs of 0.8 mm in thickness. The labels employed hereafter for the experimental groups can also be found in Table 5. The mixing of bimodal mixtures (and of the unimodal powders for homogenization after sieving) was conducted in a cylindrical drum in a Roto-Shake Genie equipment at 16 rpm to promote radial and axial mixing for 2 h in the horizontal position and 2 h in the vertical position, while changing between them at 1 h intervals.

The size distributions of the as-delivered powders (controls) of the sieved fractions and of the mixtures were measured using laser diffraction. A classic diffraction arrangement with a parallel beam path (HELOS, Sympatec GmbH, Clausthal-Zellerfeld, Germany) in combination with a dry dispersion unit with an aerosol free jet (RODOS, Sympatec GmbH) and a microdosing unit for feeding very small quantities of dry substances (ASPIROS, Sympatec GmbH) were used for this purpose. The optical structure is in accordance with ISO 13 320. Three separate runs were conducted using an R3 Lens or an R5 Lens in order to detect particles in the small range and larger range, respectively. The diffraction data were analyzed using the parameter-free Fraunhofer model. The accuracy of the measuring system is specified by the manufacturer with an average relative standard deviation to the absolute value smaller than 1% and a maximum relative deviation smaller than 2.5%.

Powder Pressing and Specimen Fabrication: From each set of specimens, discs and beams were produced by dry pressing (see Figure 10a,b) with custom-fabricated hardened steel molds with oversized dimensions accounting for a posterior linear shrinkage of about 20%. For biaxial flexural strength, discs specimens were pressed in order to obtain sintered discs having final dimensions of $12.2 \pm 0.02\ \text{mm}$ in diameter and either $0.8 \pm 0.01\ \text{mm}$ or $2.0 \pm 0.01\ \text{mm}$ in thickness by pouring 0.65 or 1.50 g of powder, respectively. The powders were poured into the mold, lightly hand vibrated (not tapped) for obtaining a uniformly spatially distributed powder bed, and subsequently cold uniaxial pressed with 222 MPa and 10 s dwell time. Beams intended for uniaxial flexural tests having final dimensions height (W) \times width (B) and length (L) of $3\ \text{mm} \times 4\ \text{mm} \times 50\ \text{mm}$ were produced by pouring 3.65 g of powder, lightly vibrated to obtain a uniform powder height in the mold, and cold uniaxial pressed with 98 MPa and 10 s dwell time (Figure 10d). Subsequently, all specimen

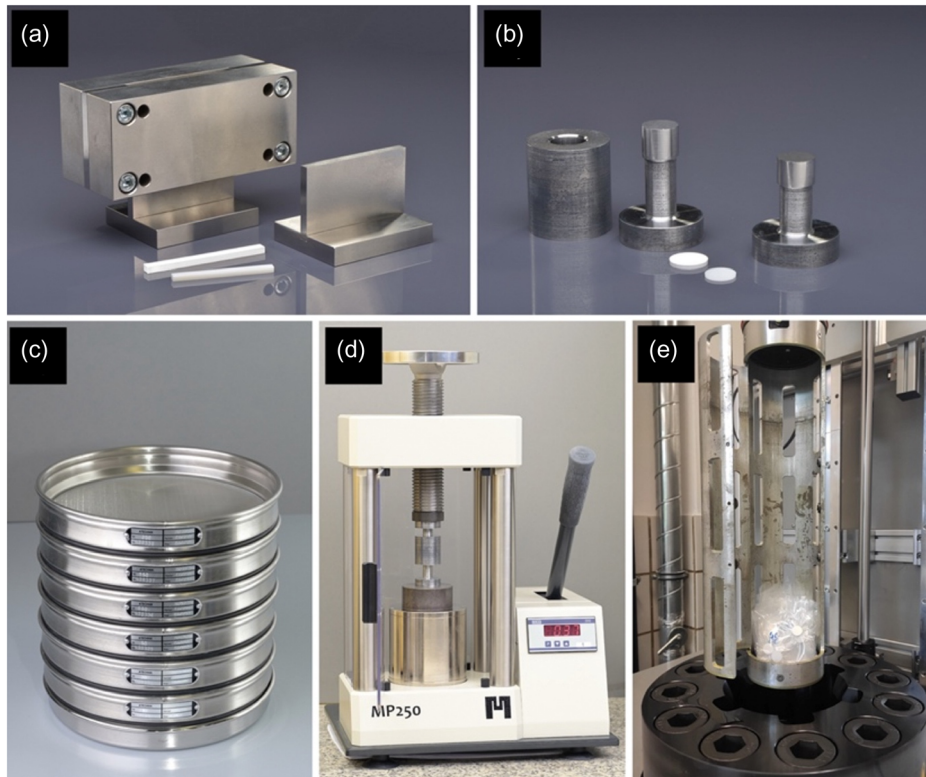


Figure 10. Images showing several steps of specimen fabrication procedures. a) Mold used to fabricate beams for uniaxial flexure; b) mold used for fabrication of discs intended for biaxial flexure; c) sieve system used to partition the powder fractions; d) manual press used for prepressing of specimen in the molds; and e) cold-isostatic pressing conducted after the prepressing.

Table 4. Weight percentage of the respective sieved fractions obtained from a 1 kg package of the commercial Tosoh 3YSZ and 5YSZ feedstocks. In labels, $x = 3$ or 5.

Partitioned fractions	3YSZ [Control Powder]	5YSZ [Control Powder]
	Weight fraction [%]	Weight fraction [%]
Label xY_11 [range 11–20 μm]	0.59 \pm 0.24	0.98 \pm 0.15
Label xY_20 [range 20–50 μm]	25.3 \pm 1.8	26.3 \pm 5.1
Label xY_50 [range 50–100 μm]	73.5 \pm 3.5	58.5 \pm 6.9
Label xY_100 [range 100–150 μm]	0.59 \pm 0.41	14.6 \pm 2.2
Label xY_150 [range 150–200 μm]	0	0.58 \pm 0.37

Table 5. Experimental mixtures of the sieved fractions (in wt%) used for fabrication of flexural specimens.

Mixtures of the partitioned fractions	3YSZ	5YSZ
	Weight fraction [%] in the mixture	Weight fraction [%] in the mixture
Label xY_20	100%	100%
Label xY_50	100%	100%
Label xY_20 + 50	25% + 75%	25% + 75%
Label 3Y_11 + 100	25% + 75%	–
Label 5Y_20 + 100	–	25% + 75%
Label 5Y_11 + 150	–	65% + 35%

geometries were submitted to cold isostatic pressing (CIP) under 300 MPa for 60 s (Figure 10e).

The specimens were sintered according to a protocol recommended by Tosoh, namely, heating with a heat rate of 5 K min⁻¹ to 300 °C, with 10 K min⁻¹ to 700 °C, and with 2 K min⁻¹ to 1000 °C and holding time of 1 h; further heating with a heat rate of 10 K min⁻¹ to the final temperature of 1450 °C for 2 h dwell time, with cooling inside the furnace overnight. Debinding events occurred at 250 and 700 °C, as determined by thermogravimetry and differential scanning calorimetry (not shown).

Density Measurements: The bulk density of the sintered specimens was determined by means of buoyancy weighing following the Archimedes' principle in accordance with DIN ISO 632-2. The mass of a specimen is determined dry (m_1), under water (m_2), and wet (m_3). The bulk density

ρ_b is given by $\rho_b = (m_1 \times \rho_{\text{liq}}) / (m_3 - m_2)$, where ρ_{liq} is the density of water. Results are shown in Supporting Information.

Multiscale Fracture Toughness Testing: Five CIPped 50 mm-long beams per experimental group were presintered at 1000 °C for 1 h and cooled down to room temperature, in order to increase their handling resistance while retaining easy machinability for notching. The long beams were sawed in half to double the specimen number and subsequently notched at the midsection with a thin 0.15 mm-thick diamond disc according to the Chevron-notched-beam (CNB) method following the guidelines of ASTM C1421.^[46] The notched presintered specimens were then fully sintered (2 h at 1450 °C) with the notch tip directed upward in the oven and grinded plane parallel under water irrigation to remove any eventual slight warping.

Prior to testing, the specimens were dried in an oven at 150 °C together with a silicon oil bath, into which the specimens were immersed after 3 h with the aim of protecting against environmental exposure thus minimizing slow crack growth effects^[47] during the test. Specimens were tested at a loading rate of 0.05 mm s⁻¹ in a fully articulated self-aligning custom testing jig^[48,49] in four-point bending (4PB) with 10–20 mm spans. The individual load-line displacement was recorded on the specimen's surface while illuminated by a laser beam and controlled by an imaging system (LaserXtens, Zwick/Roell, Germany) based on the Speckle correlation approach. This enabled detection of the stable crack growth before instability and resolving test validity. For valid load–displacement curves showing subcritical crack pop-in, the fracture toughness K_{Ic} was calculated from the maximum force at fracture F_{max} ^[46]

$$K_{I,c} = \frac{F_{max}(S_o - S_i)}{BW^{3/2}} \times \frac{Y_{min}^*}{\sqrt{10^3}} \quad (13)$$

being S_o and S_i the outer and inner span lengths, respectively, with

$$Y_{min}^* = \frac{0.3874 - 3.0919(l_0/W) + 4.2017(l_1/W) - 2.3127(l_1/W)^2 + 0.6379(l_1/W)^3}{1 - 2.9686(l_0/W) + 3.5056(l_0/W)^2 - 2.1374(l_0/W)^3 + 0.0130(l_1/W)} \quad (14)$$

where l_0 is the distance between the bottom edge of the beam and the tip of the Chevron notch, and l_1 is an arithmetic mean of the notched segments on the sides of the beam. The ratios l_0/W and l_1/W were kept within the ranges $0.175 < l_0/W < 0.225$ and $0.95 < l_1/W < 1$. The measure l_0 was obtained after fracture using in a stereomicroscope coupled with a digital camera and accompanying software. Our CNB testing procedures have been validated using a Standard Reference Material and shown consistency for zirconia and other ceramic-based materials.^[50]

For the 3Y_Control and 5Y_Control groups, two $3 \mu\text{m} \times 3 \mu\text{m} \times 12 \mu\text{m}$ μ -cantilever fracture toughness specimens were produced with an additional FIB notch of a depth of about 20–30% the cantilever beam height (W). The notch was milled with a small ion current of 20 pA and before the final side polishing of the cantilever, in order to exclude any FIB curtaining effects. Due to the small size of the fracture samples,^[51,52] an elastic–plastic fracture mechanics protocol was used to evaluate the J -Integral and R-curve of the specimen^[53]

$$J_I = J_{I,el} + J_{I,pl} = \frac{K_I(1 - \nu^2)}{E} + \frac{\eta A_{pl}}{B(W - a)} \quad (15)$$

with $J_{I,el}$ being the elastic part, and $J_{I,pl}$ the plastic part of the J -Integral. The Young's modulus E is 214 GPa, and the Poisson's ratio ν is 0.314 for both materials.^[32] The parameter η is calculated throughout the experiment according to Kolednik et al,^[54] and A_{pl} is the area under the load–displacement relative to the plastic work.^[55] The linear-elastic stress intensity factor term K_I is calculated using

$$K_I = \frac{FL}{BW^{3/2}} \times f\left(\frac{a}{W}\right) \quad (16)$$

where L stands for the distance between the notch and the loading point, and the geometry factor $f(a/W)$ being^[56]

$$f\left(\frac{a}{W}\right) = 4 \frac{3(a/W)^{0.5}[1.23 - (a/W)(1 - a/W)] - [-6.09 + 13.96\left(\frac{a}{W}\right) - 14.05(a/W)^2]}{2[1 + 2(a/W)][1 - (a/W)^{1.5}]} \quad (17)$$

Here, the continuous stiffness measurement (CSM) option of the FT-NMT03 Nanoindenter was used to continuously track the cantilever stiffness and calculate the crack length throughout the experiment using the model of Alfreider et al.^[57] Therefore, a continuous evaluation of the J -Integral is possible using the standard equations.^[54,56,58]

Multiscale Strength Testing: Testing for the Weibull strength size effect, strength tests were conducted across multiple size scales of specimens within the macro- and microscopic range. The specimens' effective surfaces and volumes were varied by changing the testing configuration or specimens' dimensions. For bending beams tested in 4PB, specimens having $B \times W \times L$ of 3 mm \times 4 mm \times 50 mm were tested in the 20/40 mm spans, and the further testing of their fractured halves was performed in the 10/20 mm spans. For the 3YSZ material, 50 mm-long beams were tested in 3PB with 20 mm span; the resulting fractured halves were further tested in the same configuration. Discs for biaxial flexural tests were varied in final thickness t , having either 0.8 or 2.0 mm.

The uniaxial flexural strength for the 4PB beams was calculated using standard beam solutions (whether in the 20–40 mm span or 10–20 mm spans), i.e.

$$\sigma_{f,4PB} = \frac{3S_o F_{max}}{4BW^2} \quad (18)$$

The biaxial flexural strength was measured using the Ball-on-Three-Balls (B3B) method using the Leoben jig that allows for ball rolling thus minimizing ball-specimen friction with accompanying stress solutions.^[59] The maximum principal stress that develops on the tensile side of the specimen at fracture is taken as the strength at fracture, calculated from

$$\sigma_{f,B3B} = \delta \frac{F_{max}}{t^2} \quad (19)$$

with t being the thickness of the specimen, F_{max} the force at fracture, and δ a function derived using finite element analysis dependent on the Poisson's ratio of the material ($\nu = 0.314$ ^[32]) and the ratios of the specimen dimensions (thickness t and specimen radius R) to the support radius, R_s ^[60]

$$\delta\left(\frac{t}{R_s}, \frac{R}{R_s}, \nu\right) = \exp\left[0.697(1 + \nu) - 0.118 \ln \frac{t}{R_s} - 0.728 \sqrt{\frac{Rt^2}{R_s^3}}\right] k_1 k_2 \quad (20)$$

where the support radius $R_s = 2R_b/\sqrt{3}$ is formed by the three supporting balls of $R_{sb} = 4$ mm. The change in maximum stress due to the increase in contact radius between specimen and loading ball is accounted for by the correction factor k_1 ^[60]

$$k_1 = 1.0052 + 0.00063 \ln(R_c/R_s \times t/R_s) - 0.5928 \frac{(R_c/R_s)^{1.6756}}{(t/R_s)^{1.3523}} \quad (21)$$

$$R_c = \sqrt[3]{\frac{3PR_{lb}}{4} \left(\frac{1 - \nu^2}{E} + \frac{1 - \nu_{lb}^2}{E_{lb}}\right)} \quad (22)$$

with R_c being the relative contact radius of the loading ball with the compression side of the specimen. E is the elastic modulus ($E_{zr} = 215$ GPa^[32]) (subscript lb = hardened stainless steel 42 °C loading ball, $E_{lb} = 200$ GPa, $\nu = 0.24$). The shift in the contact point between the supporting balls and specimen, which change the bending moment during loading, is corrected by the factor k_2 ^[60]

$$k_2 = 1 + \frac{\sqrt{3} P}{2 E t^2} \left[(1 - \nu^2) \frac{R/R_s}{t/R_s} \left(0.0015 - 1.13 \frac{1}{(R/R_s)^2} \right) \right] \quad (23)$$

Friction between specimen and supporting balls is estimated to be $< 1\text{--}2\%$ for our specimen thicknesses and elastic modulus.

Quasi-static tests for the 4PB and B3B tests were performed using a universal testing machine (Z2.5, Zwick/Roell, Ulm, Germany), in air with a controlled relative humidity of $40 \pm 2\%$ at 23 ± 2 °C and a high traverse displacement rate of 1.5 mm min⁻¹ to minimize environmental effects.

For the 3Y_Control and 5Y_Control groups, five micro-sized cantilever (μ -cantilever) specimens were produced by focused-ion beam (FIB) milling (from broken pieces of the 4PB beams) in the sizes $W \times B \times L$

of $3\ \mu\text{m} \times 3\ \mu\text{m} \times 12\ \mu\text{m}$ (lever length $S = 10\ \mu\text{m}$) and $W \times B \times L$ of $10\ \mu\text{m} \times 10\ \mu\text{m} \times 35\ \mu\text{m}$ (lever length $S = 30\ \mu\text{m}$) with a Ga^+ -ion beam currents of between 15 nA (coarse cuts) to 300 pA (last polishing step) at 30 kV. The μ -cantilever specimens were tested in situ inside a Zeiss Crossbeam 1540 EsB FIB-SEM using a FemtoTools FT-NMT03 Nanoindenter in a displacement-controlled setup. A diamond wedge indenter was used, and the strain rate was set to $0.001\ \text{s}^{-1}$ (same as for the micro fracture toughness experiments). The flexural stress at fracture was obtained by^[61]

$$\sigma_{f,\mu\text{-cant}} = \frac{6SF_{\text{max}}}{BW^2} \quad (24)$$

with S being the distance between the base and the indenter tip at the loading point.

Datasets of 20–40 specimens for the macro-sized specimens and 2–3 specimens for the μ -cantilevers were tested. The strength data were analyzed using two-parameter Weibull statistics corrected by the number of specimens in order to obtain the characteristic strength (σ_0) and Weibull modulus (m) through the maximum likelihood estimation procedure.

μ -Computer Tomography: In an effort to directly measure defect sizes in the sintered samples, disc specimens of 0.8 mm thickness from groups 3Y_Control, 5Y_Control, 3Y_11 + 100, and 5Y_11 + 150 were selected and sawed to obtain a $1\ \text{mm} \times 1\ \text{mm} \times 0.8\ \text{mm}$ parallelepiped section from the center. Subsequently, they were scanned using a μ -Computer Tomograph GE Phoenix v|tome|x s 240. The scanning process employed an 180NF nano-tube operating at 110 kV voltage and 100 μA current, with collimation and Cu-filter set at 0.1 mm and a scan resolution of 2 μm . The samples were reconstructed with the aid of the proprietary software GE datos|x v.2.4.0 using Feldkamp algorithm for cone beam X-ray CT. The three-dimensional volume was analyzed using the software package VolumeGraphics Studio MAX 3.1 to show the defects. The size and frequency of such defects were then evaluated for each sample within the entire material volume scanned by the algorithm “VGDefX”. Due to beam hardening artifacts from the scanning, an $\approx 50\ \mu\text{m}$ -thick zone on the edges of the samples were excluded from the analysis. All defects detected by the software algorithm were checked individually to remove false porosities (usually $< 3\ \mu\text{m}$) as interpreted by the software due to weak contrast and scanning artifacts in the bulk material.

Supporting Information

Supporting Information is available from the Wiley Online Library or from the author.

Acknowledgements

This work was supported by FAPESP grant no. 2022/08594-6 for author R.M.P. The authors thank Tanja Lube for insightful discussions and valuable advice, and Petra Fengler for the accurate measurements of particle distributions.

Open Access funding enabled and organized by Projekt DEAL.

Conflict of Interest

The authors declare no conflict of interest.

Data Availability Statement

The data that support the findings of this study are available from the corresponding author upon reasonable request.

Keywords

powder processing, pressing defects, strength, Weibull statistics, zirconia ceramics

Received: January 19, 2024

Revised: April 16, 2024

Published online:

- [1] S. Tanaka, C. Chia-Pin, Z. Kato, K. Uematsu, *J. Eur. Ceram. Soc.* **2007**, *27*, 873.
- [2] S. Tanaka, C. C. Pin, K. Uematsu, *J. Am. Ceram. Soc.* **2006**, *89*, 1903.
- [3] Y. Zhang, T. Suga, M. Kawasaki, X. X. Tang, N. Uchida, K. Uematsu, *J. Am. Ceram. Soc.* **1996**, *79*, 435.
- [4] T. Hondo, K. Yasuda, F. Wakai, S. Tanaka, *J. Eur. Ceram. Soc.* **2018**, *38*, 1846.
- [5] G. Okuma, S. Watanabe, K. Shinobe, N. Nishiyama, A. Takeuchi, K. Uesugi, S. Tanaka, F. Wakai, *Sci. Rep.* **2019**, *9*, 11595.
- [6] A. Boursier, G. G. d'Esdra, E. Lintingre, C. Fretigny, F. Lequeux, L. Talini, *Ceram. Int.* **2020**, *46*, 9680.
- [7] R. Lapovok, D. Tomus, C. Bettles, *Scr. Mater.* **2008**, *58*, 898.
- [8] P. Höhne, B. Mieller, T. Rabe, *Int. J. Appl. Ceram. Technol.* **2020**, *17*, 2212.
- [9] P. Höhne, B. Mieller, T. Rabe, *J. Ceram. Sci. Technol.* **2018**, *9*, 327.
- [10] M. Stuer, Z. Zhao, P. Bowen, *J. Eur. Ceram. Soc.* **2012**, *32*, 2899.
- [11] Y. F. Zhang, J. Binner, C. Rielly, B. Vaidhyanathan, *J. Eur. Ceram. Soc.* **2014**, *34*, 1001.
- [12] J. Fruhstorfer, C. G. Aneziris, *Ceram. Int.* **2017**, *43*, 13175.
- [13] T. Yano, S. Ohsaki, H. Nakamura, S. Watano, *Adv. Powder Technol.* **2021**, *32*, 1362.
- [14] J. Schmidt, E. J. R. Parteli, N. Uhlmann, N. Wörlein, K. E. Wirth, T. Pöschel, W. Peukert, *Adv. Powder Technol.* **2020**, *31*, 2293.
- [15] R. Belli, U. Lohbauer, *J. Am. Ceram. Soc.* **2021**, *104*, 4819.
- [16] W. J. Walker, J. S. Reed, S. K. Verma, *J. Am. Ceram. Soc.* **1999**, *82*, 1711.
- [17] X. J. Ye, Y. P. Li, Y. L. Ai, Y. Nie, *Adv. Powder Technol.* **2018**, *29*, 2280.
- [18] H. J. Frost, R. Raj, *J. Am. Ceram. Soc.* **1982**, *65*, C19.
- [19] G. D. Scott, *Nature* **1960**, *188*, 908.
- [20] F. Zok, F. F. Lange, J. R. Porter, *J. Am. Ceram. Soc.* **1991**, *74*, 1880.
- [21] R. M. German, *Metall. Trans. A* **1992**, *23*, 1455.
- [22] J. Fruhstorfer, J. Hubáľková, C. G. Aneziris, *J. Eur. Ceram. Soc.* **2019**, *39*, 3264.
- [23] J. W. Oh, S. K. Ryu, W. S. Lee, S. J. Park, *Powder Technol.* **2017**, *322*, 1.
- [24] W. C. Du, M. Singh, D. Singh, *Ceram. Int.* **2020**, *46*, 19701.
- [25] S. Gallops, T. Fett, J. J. Kruzic, *J. Am. Ceram. Soc.* **2011**, *94*, 2556.
- [26] S. Funkschilling, T. Fett, M. J. Hoffmann, R. Oberacker, T. Schwind, J. Wippler, T. Bohlke, H. Ozcoban, G. A. Schneider, P. F. Becher, J. J. Kruzic, *Acta Mater.* **2011**, *59*, 3978.
- [27] J. J. Kruzic, R. L. Satet, M. J. Hoffmann, R. M. Cannon, R. O. Ritchie, *J. Am. Ceram. Soc.* **2008**, *91*, 1986.
- [28] J. W. Foulk, G. C. Johnson, P. A. Klein, R. O. Ritchie, *J. Mech. Phys. Solids* **2008**, *56*, 2381.
- [29] T. Fett, *New Contributions to R-Curves and Bridging Stresses – Applications of Weight Functions*, KIT Scientific Publishing, Karlsruhe **2012**.
- [30] B. Basu, J. Vleugels, O. Van der Biest, *Mater. Sci. Eng. A* **2004**, *380*, 215.
- [31] A. Smirnov, H. D. Kurland, J. Grabow, F. A. Muller, J. F. Bartolome, *J. Eur. Ceram. Soc.* **2015**, *35*, 2685.
- [32] R. Belli, K. Hurler, J. Schürlein, A. Petschelt, K. Werbach, H. Peterlik, T. Rabe, B. Mieller, U. Lohbauer, *J. Eur. Ceram. Soc.* **2021**, *41*, 7771.
- [33] D. Munz, *J. Am. Ceram. Soc.* **2007**, *90*, 1.

- [34] A. Schellenberger, R. Belli, J. Karsten, U. Lohbauer, *Eng. Fract. Mech.* **2023**, 291, 109527.
- [35] R. Danzer, T. Lube, P. Supancic, R. Damani, *Adv. Eng. Mater.* **2008**, 10, 275.
- [36] M. Staudacher, A. Eggel, P. Supancic, T. Lube, *J. Eur. Ceram. Soc.* **2024**, 44, 173.
- [37] G. D. Quinn, *J. Am. Ceram. Soc.* **2003**, 86, 508.
- [38] M. Staudacher, T. Lube, J. Glettler, U. Scheithauer, M. Schwentenwein, *J. Eur. Ceram. Soc.* **2023**, 15, 100410.
- [39] R. Danzer, P. Supancic, J. Pascual, T. Lube, *Eng. Fract. Mech.* **2007**, 74, 2919.
- [40] R. Danzer, *J. Eur. Ceram. Soc.* **2006**, 26, 3043.
- [41] R. Danzer, T. Lube, P. Supancic, *Z. Metallkd.* **2001**, 92, 773.
- [42] R. Danzer, T. Lube, in *Ceramic Materials and Components FOR Engine* (Ed: K. Niihara et al.), Japan Fine Ceramics Association, Tokyo **1998**, pp. 683–688.
- [43] D. Munz, T. Fett, *Ceramics: Mechanical Properties, Failure Behaviour, Materials Selection*, Springer, Berlin **1999**.
- [44] EN 843-5, *Mechanical Testing of Monolithic Ceramics at Room Temperature. Part 5: Statistical Treatment*, CEN European Committee for Standardization **1997**.
- [45] T. Klünsner, S. Wurster, P. Supancic, R. Ebner, M. Jenko, J. Glätzle, A. Püschel, R. Pippan, *Acta Mater.* **2011**, 59, 4244.
- [46] ASTM C1421, *Standard Test Methods for Determination of Fracture Toughness of Advances Ceramics at Ambient Temperature*, ASTM International **2010**.
- [47] C. Krautgasser, Z. Chlup, P. Supancic, R. Danzer, R. Bernejo, *J. Eur. Ceram. Soc.* **2016**, 36, 1307.
- [48] R. Belli, M. Wendler, J. I. Zorzin, U. Lohbauer, *Dent. Mater.* **2018**, 34, 97.
- [49] J. Lubauer, U. Lohbauer, M. Henrich, M. Munz, T. Lube, R. Belli, *J. Am. Ceram. Soc.* **2022**, 105, 7582.
- [50] R. Belli, M. Wendler, A. Petschelt, T. Lube, U. Lohbauer, *J. Eur. Ceram. Soc.* **2018**, 38, 5533.
- [51] R. Pippan, S. Wurster, D. Kiener, *Design* **2018**, 159, 252.
- [52] M. Wurmshuber, M. Alfreider, S. Wurster, M. Burtscher, R. Pippan, D. Kiener, *Acta Mater.* **2023**, 250.
- [53] ASTM E1820, *Standard Test Method for Measurement of Fracture Toughness*, ASTM International **2013**.
- [54] O. Kolednik, M. Sistaninia, S. Kolitsch, *Eng. Fract. Mech.* **2023**, 292, 109636.
- [55] X. K. Zhu, J. A. Joyce, *Eng. Fract. Mech.* **2012**, 85, 1.
- [56] S. Wurster, C. Motz, R. Pippan, *Philos. Mag.* **2012**, 92, 1803.
- [57] M. Alfreider, S. Kolitsch, S. Wurster, D. Kiener, *Mater Des.* **2020**, 194, 108914.
- [58] M. Alfreider, D. Kozic, O. Kolednik, D. Kiener, *Mater Des.* **2018**, 148, 177.
- [59] A. Börger, P. Supancic, R. Danzer, *J. Eur. Ceram. Soc.* **2002**, 22, 1425.
- [60] M. Staudacher, T. Lube, P. Supancic, *J. Eur. Ceram. Soc.* **2023**, 43, 648.
- [61] E. Carrera, G. Giunta, M. Petrolo, *Beam Structures: Classical and Advanced Theories*, Wiley, Hoboken, NJ **2011**.